

## Statistical physics of the development of Kerner's synchronized-to-free-flow instability at a moving bottleneck in vehicular traffic

Vincent Wiering <sup>1</sup>, Sergey L. Klenov,<sup>2</sup> Boris S. Kerner <sup>1</sup> and Michael Schreckenberg<sup>1</sup>

<sup>1</sup>*Physik von Transport und Verkehr, Universität Duisburg-Essen, 47048 Duisburg, Germany*

<sup>2</sup>*Moscow Institute of Physics and Technology, Department of Physics, 141700 Dolgoprudny, Moscow Region, Russia*



(Received 8 June 2022; accepted 14 September 2022; published 10 November 2022)

With the use of simulations of a stochastic microscopic traffic model in the framework of the three-phase traffic theory, we have revealed the statistical physics of a traffic flow instability with respect to a transition from synchronized flow (S) to free flow (F) (Kerner's  $S \rightarrow F$  instability) at a moving bottleneck (MB) occurring through a slow-moving vehicle in vehicular traffic. We have found that the  $S \rightarrow F$  instability can occur at the MB more frequently than at an on-ramp bottleneck. From a comparison of the occurrence of the  $S \rightarrow F$  instability at the MB and on-ramp bottleneck at the same probability of traffic breakdown and the same flow rate it has been found that, whereas the frequency of the  $S \rightarrow F$  instability at the on-ramp bottleneck barely changes, the larger the velocity of the MB, the more frequently the  $S \rightarrow F$  instability occurs at the MB. Contrarily, when the MB velocity decreases considerably, then rather than the  $S \rightarrow F$  instability, in synchronized flow at the MB the classical traffic flow instability leading to the emergence of wide-moving jams ( $S \rightarrow J$  instability) occurs. It has been found that the physics of the intensification of the  $S \rightarrow F$  instability at the MB with the increase in the MB velocity is associated with the increase in the mean space gap (mean time headway) between vehicles in synchronized flow. For this reason, when the MB velocity increases, there is an MB velocity at which the  $S \rightarrow F$  instability dominates the  $S \rightarrow J$  instability: The MB velocity influences considerably on the competition between the  $S \rightarrow F$  and classical traffic flow instabilities in synchronized flow.

DOI: [10.1103/PhysRevE.106.054306](https://doi.org/10.1103/PhysRevE.106.054306)

### I. INTRODUCTION

The classical traffic flow instability in vehicular traffic flow introduced in 1958 by Herman and colleagues from the General Motors (GM) Company [1–4] as well as by Kometani and Sasaki [5–8] is up to now a subject of intensive empirical and theoretical studies in vehicular traffic science (e.g., papers, reviews and books [9–24]). The classical traffic instability was incorporated into a number of traffic flow models which can be considered belonging to the same GM model class. As found in 1994 [25,26], the classic instability leads to a phase transition from free flow to wide-moving jam ( $F \rightarrow J$  transition).

However, the  $F \rightarrow J$  transition cannot explain traffic breakdown (the onset of traffic congestion) observed in real data: In all empirical traffic data measured at real highways traffic breakdown is a transition from free flow to synchronized flow ( $F \rightarrow S$  transition) that occurs in metastable free flow with respect to an  $F \rightarrow S$  transition at a bottleneck [27,28]. In other words, the  $F \rightarrow S$  transition exhibits the empirical nucleation nature. To explain the empirical nucleation nature of traffic breakdown ( $F \rightarrow S$  transition), Kerner introduced the three-phase traffic theory [27–29] (see for a review [30–33]). The three-phase traffic theory describes empirical traffic data in space and time by introducing three fundamentally different traffic phases: free flow (F), synchronized flow (S), and wide-moving jam (J); the traffic phases S and J belong to congested traffic. In the three-phase traffic theory, rather than traffic

breakdown, the classic traffic flow instability is an  $S \rightarrow J$  instability that explains the transition from synchronized flow to a wide-moving jam ( $S \rightarrow J$  transition) observed in empirical synchronized flow.

In the three-phase traffic theory, the nucleation nature of traffic breakdown ( $F \rightarrow S$  transition) is governed by a so-called  $S \rightarrow F$  instability introduced by Kerner [34]. Contrary to the classical traffic flow instability ( $S \rightarrow J$  instability) that is a growing wave of a local speed *decrease* in synchronized flow, Kerner's  $S \rightarrow F$  instability is a growing wave of a local speed *increase* in synchronized flow. The growth of this speed wave, i.e., the development of the  $S \rightarrow J$  instability leads to an  $S \rightarrow J$  transition (wide-moving jam emergence in synchronized flow). The  $S \rightarrow F$  instability exhibits a nucleation nature: Only a large enough local speed increase in an initial synchronized flow can grow whereas a low enough local speed increase decays over time in synchronized flow. In [34] it has been shown that this nucleation nature of the  $S \rightarrow F$  instability governs the nucleation nature of traffic breakdown ( $F \rightarrow S$  transition) in metastable free flow with respect to the  $F \rightarrow S$  transition. In an empirical example shown in Figs. 1(a) and 1(b), both traffic breakdown ( $F \rightarrow S$  transition) and the  $S \rightarrow J$  transition can be clearly seen. In the three-phase traffic theory [30–32], both the nucleation nature of the  $S \rightarrow F$  instability and the nucleation nature of the  $F \rightarrow S$  transition are explained by a discontinuous character of over-acceleration probability in vehicular traffic that is qualitative shown in Fig. 1(c). Traffic breakdown ( $F \rightarrow S$  transition) governed by

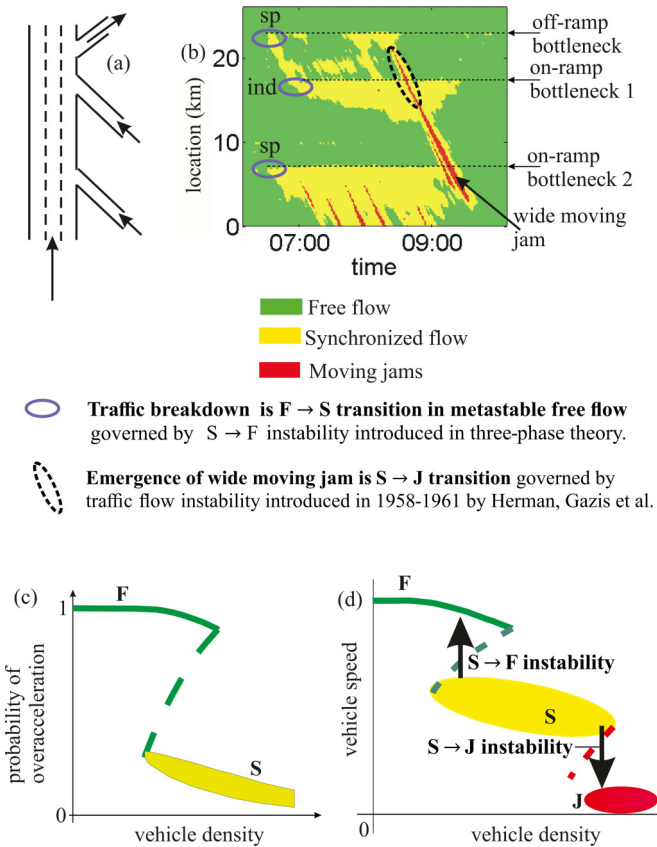


FIG. 1. A known empirical example of phase transitions in traffic flow illustrating two traffic flow instabilities of three-phase theory (real measured traffic data of road detectors installed along a three-lane highway) (a), (b) [30] and illustrations of associated hypotheses of three-phase theory (c), (d). (a) Sketch of section of three-lane highway with three bottlenecks. (b) Speed data measured with road detectors installed along road section in (a); data [30] are presented in space and time with averaging method described in Sec. C.2 of [35]. (c) Hypothesis of three-phase theory about the discontinuous character of over-acceleration probability [27,28,30,31]. (d) Hypothesis of three-phase theory about  $F \rightarrow S \rightarrow J$  phase transitions in traffic flow: 2Z characteristic for phase transitions [28,30]. F = free flow phase, S = synchronized flow phase, J = wide-moving jam phase. In (b), "sp" = spontaneous  $F \rightarrow S$  transition, "ind" = induced  $F \rightarrow S$  transition [30].

Kerner's  $S \rightarrow F$  instability and the  $S \rightarrow J$  transition determined by the classical traffic flow instability can also be illustrated with the use of a double Z (2Z) characteristic of phase transitions as shown in Fig. 1(d).

Recently, Kerner has found that there can be a spatiotemporal competition between the  $S \rightarrow F$  and  $S \rightarrow J$  instabilities in synchronized flow [36]. The spatiotemporal competition between the  $S \rightarrow F$  and  $S \rightarrow J$  instabilities results in the emergence of a diverse variety of spatiotemporal traffic patterns consisting of complex alternations of the three traffic phases F, S, and J.

The first implementations of the three-phase traffic theory in mathematical traffic flow models are a stochastic microscopic model [37] and a cellular automaton three-phase model

[38]. These three-phase traffic flow models have been further developed for different applications, in particular, for a study of traffic breakdown and resulting traffic congestion occurring at different road bottlenecks like on-ramp, off-ramp, and merge bottlenecks (see, e.g., [39–44]). Over time, other traffic flow models have also been developed, which incorporate some of the hypotheses of the three-phases traffic theory, as well as many new results in the framework of the three-phase traffic theory have been obtained (see, e.g., [45–83]).

Besides road bottlenecks there can also be a moving bottleneck (MB) caused by a slow-moving vehicle on a multilane road. Vehicles behind the MB have to slow down or change the lane and overtake the slow-moving vehicle. A possibility of an MB was predicted in the works by Gazis and Herman [84,85]. Newell [86,87] revealed that in a system coordinate moving at the MB velocity traffic breakdown at the MB should exhibit qualitatively the same features as those at road bottlenecks. A theory of traffic breakdown and resulting congested patterns at MBs in the framework of the three-phase traffic theory has been developed in [88]. As shown in [88], characteristics of synchronized flow at an MB resulting from traffic breakdown depends on the traffic flow and the velocity of the slow-moving vehicle that we denote by  $v_{MB}$ . Recently a study of prediction of traffic breakdown at MBs with the use of probe vehicle data has been made [89,90].

In this paper, we reveal that the  $S \rightarrow F$  instability can occur at a highway bottleneck considerably more frequently when the bottleneck is an MB. From a comparison of the occurrence of the  $S \rightarrow F$  instability at the MB and on-ramp bottleneck at the same probability of traffic breakdown and the same flow rate it has been found that, whereas the frequency of the  $S \rightarrow F$  instability at the on-ramp bottleneck barely changes, the larger the velocity  $v_{MB}$  of the MB, the more frequently the  $S \rightarrow F$  instability occurs at the MB. Contrarily, when the MB velocity  $v_{MB}$  decreases considerably, then rather than the  $S \rightarrow F$  instability, in synchronized flow at the MB the classical traffic flow instability leading to the emergence of wide-moving jams ( $S \rightarrow J$  instability) occurs. Through the use of the stochastic microscopic simulations that are based on the model of [88] we explain the physics of this vehicular traffic phenomenon.

The paper is organized as follows: A method of the physical modeling of  $S \rightarrow F$  instability at an MB used in the paper is considered in Sec. II. In Sec. III we make a study of the probability of traffic breakdown at the MB as well as compare this probability with the probability of traffic breakdown at an on-ramp bottleneck. The probabilistic features of the  $S \rightarrow F$  instability at the MB is revealed and an explanation of the physics is given in Sec. IV B. Spatiotemporal competition between  $S \rightarrow F$  and  $S \rightarrow J$  instabilities in synchronized flow at the MB are analyzed in Sec. V. In Sec. VI we discuss how a stochastic three-phase traffic flow model used in the paper for all simulations was evaluated with empirical data, explain a crucial difference between Kerner's  $S \rightarrow F$  instability and the classical traffic instability, consider differences between results of the paper with previous studies of phase transitions at an MB, discuss the chosen methodology of a comparison of phase transitions at the MB and on-ramp bottleneck, consider the role of model fluctuations in the nucleation of phase

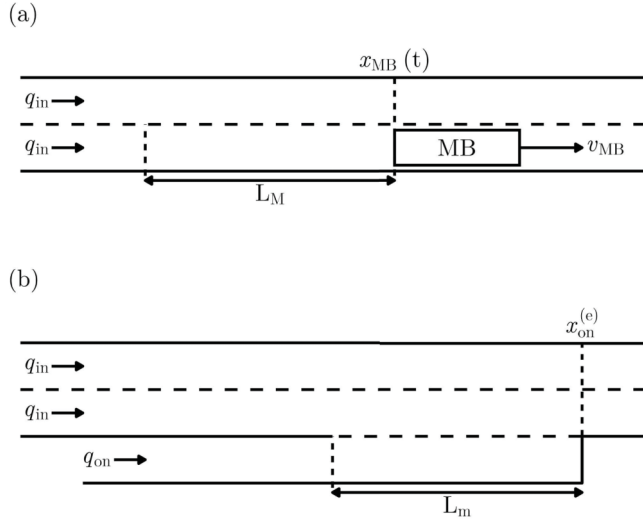


FIG. 2. Model of a moving bottleneck MB (a) and an on-ramp bottleneck (b) on a two-lane highway. At the beginning of the main lanes is a constant flow rate  $q_{in}$ . The MB is a slow-moving vehicle with constant velocity  $v_{MB}$ , which position  $x_{MB}$  changes with time  $t$ . Behind the MB is the moving merging region with length  $L_M$ , where the lane changing conditions differ from the rest of the main lanes. Vehicles appear at the beginning of the on ramp according to the constant flow rate  $q_{on}$ . Inside the merging region  $L_m$  vehicles change from the on ramp onto the main lanes. The end of the merging region and the on ramp is denoted with  $x_{on}^{(e)}$ .

transitions at the bottlenecks as well as formulate conclusion of this paper.

## II. METHOD OF PHYSICAL MODELLING OF $S \rightarrow F$ INSTABILITY AT MOVING BOTTLENECK

To analyze the statistical features of  $S \rightarrow F$  and  $S \rightarrow J$  instabilities in synchronized flow at a moving bottleneck (MB) and at an on-ramp bottleneck, we used the Kerner-Klenov Stochastic Microscopic Model (Appendix A) and simulated a two-lane highway with an MB and an on-ramp bottleneck, respectively (Fig. 2). The three traffic phases, free flow, synchronized flow, and wide-moving jam, were determined in the simulations by using the method explained in Appendix B. The flow rate  $q_{in}$  at the beginning of the main lanes, the velocity  $v_{MB}$  of the slow-moving vehicle and the flow rate  $q_{on}$  at the beginning of the on ramp as well as other simulation parameters are specified in captions to the paper's figures.

At the same model parameters,  $q_{in}$  and  $v_{MB}$  for the MB simulations and  $q_{in}$  and  $q_{on}$  for the on-ramp simulations, we made a number  $N_r$  (where  $N_r \gg 1$ ) of different realizations and checked whether traffic breakdown ( $F \rightarrow S$  transition) occurs during the observation time  $T_{ob} = 30$  min, using the method explained in Appendix C. Then the number  $n$  of realizations with traffic breakdown were counted and the probability  $P_{FS}^{(B)}$  of traffic breakdown was determined:

$$P_{FS}^{(B)} = \frac{n}{N_r}. \quad (1)$$

This was done with the MB and on-ramp bottleneck, respectively, leading to two separate probabilities of traffic breakdown,  $P_{FS,MB}^{(B)}$  for the MB and  $P_{FS,on}^{(B)}$  for the on-ramp bottleneck, which depend on the simulation parameters  $q_{in}$ ,  $v_{MB}$  and  $q_{on}$ . Features of the congested traffic at the two different bottlenecks were compared for simulation parameters, for which the traffic breakdowns showed the same probabilities  $P_{FS,MB}^{(B)}$  and  $P_{FS,on}^{(B)}$  for a certain set of parameters  $q_{in}$ ,  $v_{MB}$ , and  $q_{on}$ :

$$P_{FS,MB}^{(B)}(q_{in}, v_{MB}) = P_{FS,on}^{(B)}(q_{in}, q_{on}) = 0.5. \quad (2)$$

This condition allowed us a comparison of the congested traffic formed at the MB and on-ramp bottleneck, respectively. Of critical importance were the  $S \rightarrow F$  and  $S \rightarrow J$  instabilities, which can occur in synchronized flow and determine the behavior of congested traffic patterns. These instabilities were studied in the dependence of the velocity  $v_{MB}$  and the flow rate  $q_{on}$  under the condition from (2). Through this approach to the physical modeling we analyzed a possible competition between the  $S \rightarrow F$  and  $S \rightarrow J$  instabilities in synchronized flow occurring at the MB and at the on-ramp bottleneck.

## III. TRAFFIC BREAKDOWN ( $F \rightarrow S$ TRANSITION) AND RESULTING CONGESTED PATTERNS AT MOVING BOTTLENECK AND ON-RAMP BOTTLENECKS

### A. Comparison of probabilities of $F \rightarrow S$ transition at moving bottleneck and on-ramp bottleneck

To implement condition (2) for a finite number  $N_r$  of realization, we first determined the probabilities  $P_{FS,MB}^{(B)}$  and  $P_{FS,on}^{(B)}$  of traffic breakdown in dependence of the flow rate  $q_{in}$  at constant values of the velocity  $v_{MB}$  and flow rate  $q_{on}$  for the MB and on-ramp bottleneck, respectively. The probability  $P_{FS,on}^{(B)}$  of traffic breakdown at the on-ramp bottleneck can be fitted by a well-known function  $\tilde{P}_{FS,on}^{(B)}$  [32]:

$$\tilde{P}_{FS,on}^{(B)}(q_{in}) = (1 + e^{\alpha_{on}(q_{p,on} - q_{in})})^{-1}, \quad (3)$$

where  $\alpha_{on}$  and  $q_{p,on}$  are fit parameters. We found a similar behavior for the MB, where the probability  $P_{FS,MB}^{(B)}$  of traffic breakdown can be fitted by following function  $\tilde{P}_{FS,MB}^{(B)}$ :

$$\tilde{P}_{FS,MB}^{(B)}(q_{in}) = (1 + e^{\alpha_{MB}(q_{p,MB} - q_{in})})^{-1}, \quad (4)$$

where  $\alpha_{MB}$  and  $q_{p,MB}$  are fit parameters.

With the introduced fits  $\tilde{P}_{FS,MB}^{(B)}$  and  $\tilde{P}_{FS,on}^{(B)}$  we reformulated condition (2) into following condition:

$$q_{p,MB} = q_{p,on}. \quad (5)$$

This condition allowed us to find pairings  $(v_{MB} | q_{on})$  of MB and on-ramp bottleneck simulations, which can be used to compare the behavior of congested traffic at the MB and on-ramp bottleneck (Fig. 3).<sup>1</sup> The comparison of the two

<sup>1</sup>It is interesting to notice the strong dependence of  $\alpha_{MB}$  governing the width of the fit on the velocity  $v_{MB}$ , whereas  $\alpha_{on}$  does not change significantly with the flow rate  $q_{on}$ . Since this paper focuses on the behavior of congested traffic after the breakdown, this observation is not discussed in the paper.

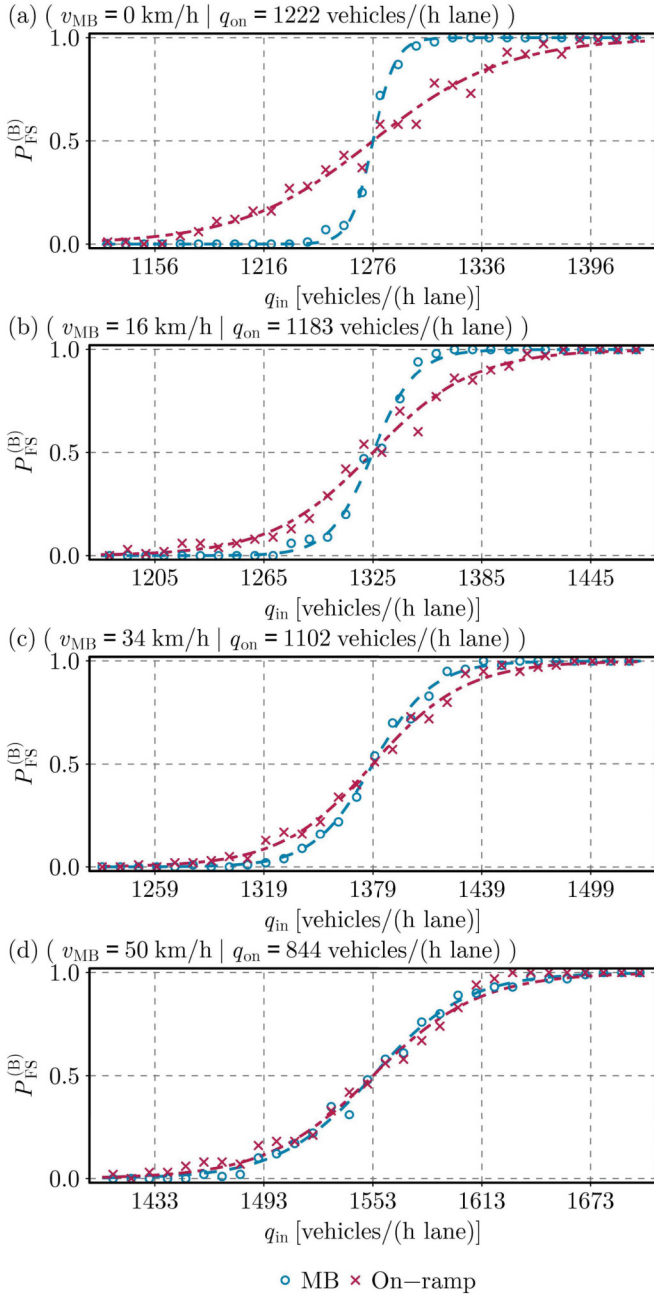


FIG. 3. Comparison of the probabilities of traffic breakdown at the MB  $P_{FS,MB}^{(B)}$  and at the on-ramp bottleneck  $P_{FS,on}^{(B)}$  as functions of the flow rate  $q_{in}$  for four examples with different velocities  $v_{MB}$  of the MB and different flow rates  $q_{on}$  of the on-ramp bottleneck. Probabilities of traffic breakdown for MB (blue circles) and on-ramp bottleneck (red crosses). Number of realizations is  $N_r = 100$  and observation time is  $T_{ob} = 30$  min. Based on the discrete points, the fit  $\tilde{P}_{FS,MB}^{(B)}$  for MB (blue, dashed line) and  $\tilde{P}_{FS,on}^{(B)}$  for on-ramp (red, dot-dashed line) from (4) and (3) was determined. The four parameters of the two fits were used to determine the pairings  $(v_{MB} | q_{on})$  according to condition (5). Model parameters used in simulations are presented in Tables A1–A3 of [32] (Appendix A of this paper); the exception is parameter  $\lambda_b$  of Table A.3 in [32] that is used in accordance with (A30).

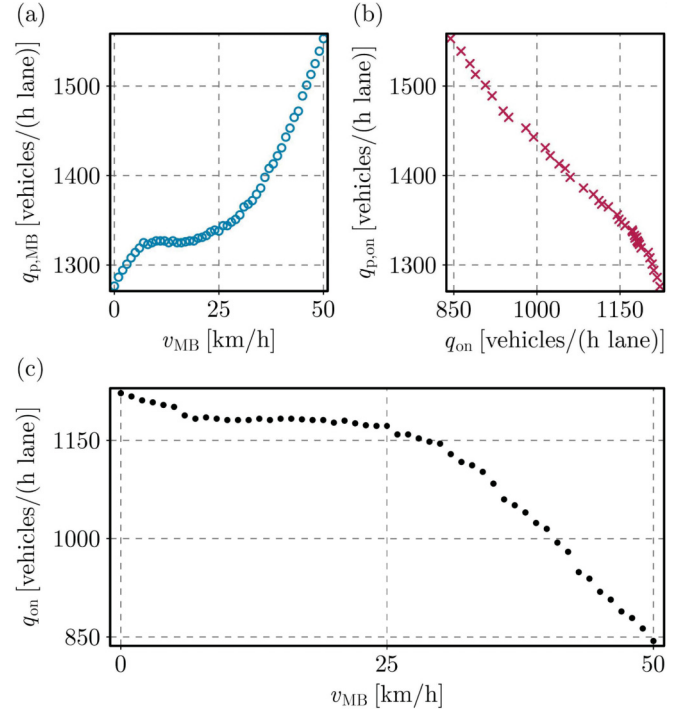


FIG. 4. In (a) we show for an MB the determined parameter  $q_{p,MB}$  from the fit  $\tilde{P}_{FS,MB}^{(B)}$  in (4) of the probability of traffic breakdown as a function of the velocity  $v_{MB}$ . Accordingly (b) shows the determined parameter  $q_{p,on}$  from the fit  $\tilde{P}_{FS,on}^{(B)}$  in (3) for an on ramp as a function of the on-ramp flow rate  $q_{on}$ . Following the condition in (5), pairings of MB and on ramp  $(v_{MB} | q_{on})$  were determined. The result is shown in (c). Other model parameters are the same as those explained in Fig. 3.

bottlenecks was done for the flow rate  $q_{in} = q_{p,MB} = q_{p,on}$  at which both probabilities  $P_{FS,MB}^{(B)}$  and  $P_{FS,on}^{(B)}$  of traffic breakdown satisfy the original condition (2).

Analysis of the  $S \rightarrow F$  and  $S \rightarrow J$  instabilities in synchronized flow was done for velocities  $v_{MB}$  of the MB between 0 km/h and 50 km/h in steps of 1 km/h. By using condition (5) each of these 51 values was assigned the flow rate  $q_{on}$  on the on-ramp bottleneck, for which the behavior of the congested traffic at the MB and on-ramp bottleneck were compared. The fit parameter  $q_{p,MB}$  increases with higher velocities  $v_{MB}$ , whereas  $q_{p,on}$  decreases with higher flow rates  $q_{on}$  [Figs. 4(a) and 4(b)]. This results in 51 pairings  $(v_{MB} | q_{on})$  of the MB and on-ramp bottleneck simulations, where the flow rate  $q_{on}$  decreases with higher velocities  $v_{MB}$  [Fig. 4(c)].

To study the  $S \rightarrow F$  and  $S \rightarrow J$  instabilities in synchronized flow we needed a high number of simulations with traffic breakdown at the bottlenecks. Therefore, for each MB and on-ramp bottleneck simulation with the parameters from Fig. 4 we examined a number  $N_r^{(B)}$  (where  $N_r^{(B)} \gg 1$ ) of realizations in which a traffic breakdown occurred during the observation time  $T_{ob} = 30$  min. After the time of the breakdown, the simulation continued for an additional observation time of  $T_{ob}^{(cong)} = 60$  min, during which the congested traffic pattern formed at the bottleneck was observed.

### B. Emergence of a diverse variety of congested traffic patterns at moving bottleneck

The velocity  $v_{MB}$  of a slow-moving vehicle representing the MB has a great influence on congested traffic patterns (congested patterns) formed at the bottleneck after traffic breakdown [88]. As found in this paper, the diverse variety of the congested patterns at the MB stems from the probabilistic behavior of  $S \rightarrow F$  and  $S \rightarrow J$  instabilities.

For low velocities  $v_{MB}$  we find general patterns (GPs) due to the  $S \rightarrow J$  instability, while for larger velocities  $v_{MB}$  we find moving synchronized flow patterns (MSPs) due to the  $S \rightarrow F$  instability [Figs. 5(a) and 5(d)]. In between these two cases exists a competition between the  $S \rightarrow F$  and  $S \rightarrow J$  instability, where both instabilities can occur inside the synchronized flow. For two different realizations with the exact same simulation parameters, we get at least two different congested patterns [Figs. 5(b) and 5(c)]. In one of the realizations an  $S \rightarrow J$  instability leads to a so-called  $S \rightarrow J \rightarrow S \rightarrow F$  transition, while in the other realizations an  $S \rightarrow F$  instability interrupts a widening synchronized flow pattern (WSP).

### C. Characteristics of synchronized flow at moving bottleneck and on-ramp bottleneck

While at the MB there is a diverse variety of congested patterns depending on the velocity  $v_{MB}$ , the same is not true for the congested patterns forming at the on-ramp bottleneck. Based on the pairings  $(v_{MB} | q_{on})$  from Fig. 4 we can see in the examples in Figs. 6 and 7 that the changing on-ramp flow rate  $q_{on}$  has a relatively small influence on the congested patterns.

For low velocities  $v_{MB}$  and high flow rates  $q_{on}$  the congested patterns forming at the respective bottlenecks are similar. For the pairing  $(0 \text{ km/h} | 1222 \text{ vehicles}/(\text{h lane}))$  we observe a GP at both bottlenecks [Fig. 6(a)]. For other examples, where the flow rate  $q_{on}$  decreases, similar GPs are observed at the on-ramp bottleneck. In contrast, the congested patterns at the MB exhibit a diverse variety for the presented parameter space. As already shown with the previous examples for the MB (Fig. 5), we observe GPs, WSPs, and MSPs, depending on the occurrences of  $S \rightarrow F$  and  $S \rightarrow J$  instabilities.

The examples (Figs. 6 and 7) show that the synchronized flow at the two different bottlenecks exhibits a very different behavior with changing parameters  $v_{MB}$  and  $q_{on}$ , although the probabilities  $P_{FS,MB}^{(B)}$  and  $P_{FS,on}^{(B)}$  of traffic breakdown and the flow rate  $q_{in}$  are equal for each pairing  $(v_{MB} | q_{on})$ .

## IV. PHYSICS OF $S \rightarrow F$ INSTABILITY IN SYNCHRONIZED FLOW AT MOVING BOTTLENECK

### A. Probability of $S \rightarrow F$ instability a moving bottleneck

An example and explanation for the  $S \rightarrow F$  instability at the MB is shown in Figs. 8 and 9. As was revealed in [36] for the on-ramp bottleneck, a speed peak with a large enough amplitude is a nuclei for an  $S \rightarrow F$  instability, which appear mostly at the vicinity of bottlenecks.

The occurrences of an  $S \rightarrow F$  instability inside synchronized flow at an MB or an on-ramp bottleneck is a stochastic process with a certain probability depending on the simulation parameters  $q_{in}$ ,  $v_{MB}$ , and  $q_{on}$ . The empirical probability  $P_{SF}$  of

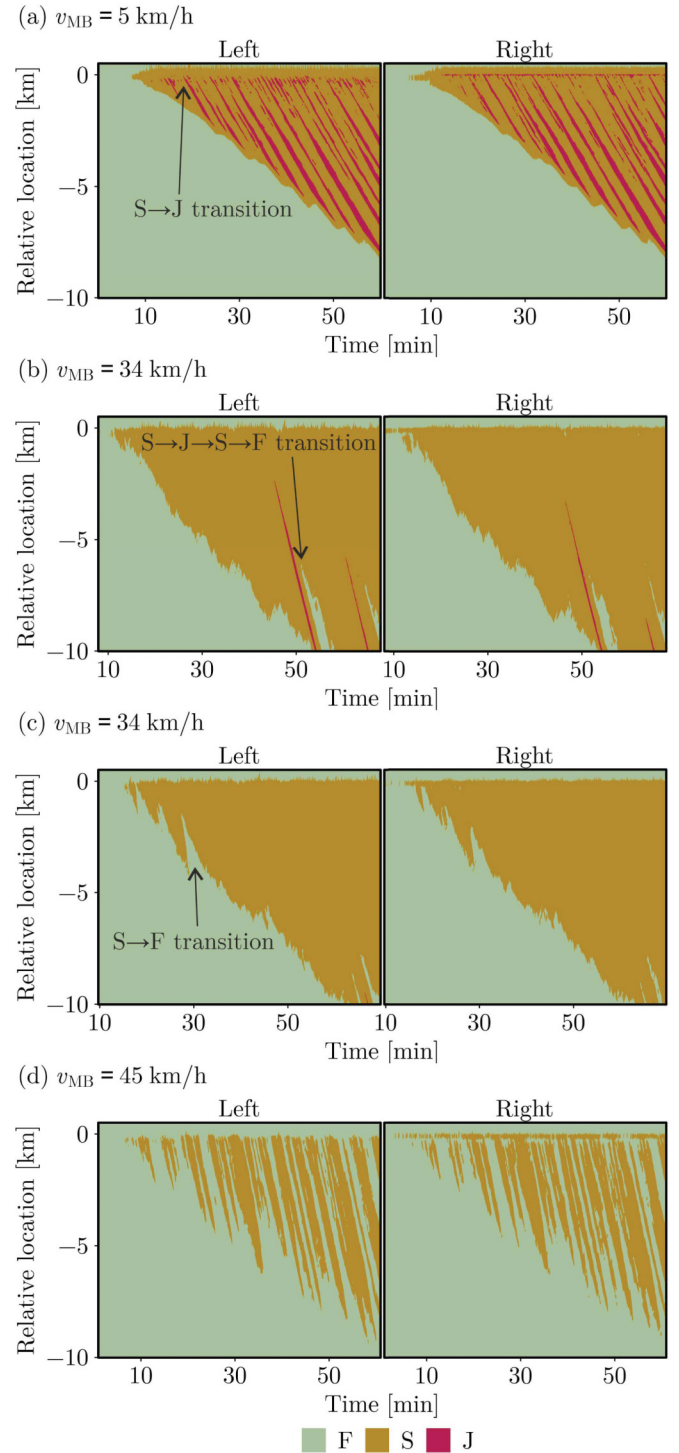


FIG. 5. Simulated traffic phases (F = free flow, S = synchronized flow, J = wide-moving jam) in time and space shown in system coordinate moving at the velocity  $v_{MB}$  for different velocities  $v_{MB}$ . The flow rate  $q_{in}$  is chosen so that condition (2) is satisfied. The flow rate  $q_{in}$  is 1314 vehicles/(h lane) (a), 1379 vehicles/(h lane) (b), (c), and 1489 vehicles/(h lane) (d). Other model parameters are the same as those explained in Fig. 3.

an  $S \rightarrow F$  instability was determined by analyzing the  $N_f^{(B)}$  realizations with a traffic breakdown for a set of the simulation parameters. During a observation time of  $T_{ob}^{(cong)} = 60 \text{ min}$  after the breakdown, we searched for  $S \rightarrow F$  and  $S \rightarrow J$

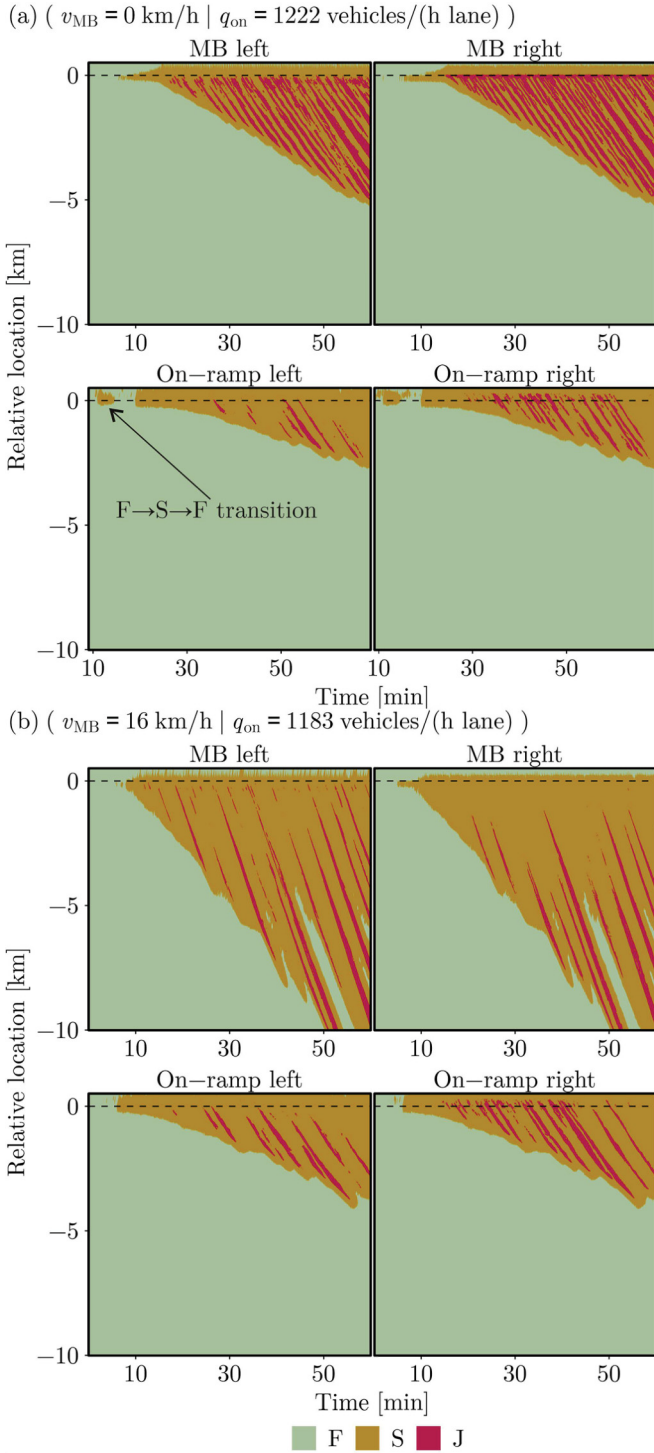


FIG. 6. Simulated traffic phases (F = free flow, S = synchronized flow, J = wide-moving jam) in time and space shown for the MB in the system coordinate moving at the velocity  $v_{MB}$  for different pairings ( $v_{MB} \mid q_{on}$ ). Panels (a) and (b) show two comparisons between MB and on ramp for the pairings ( $v_{MB} \mid q_{on}$ ) in Figs. 3(a) and 3(b). The flow rate  $q_{in}$  is chosen so that condition (2) is satisfied. The flow rate  $q_{in}$  is 1276 vehicles/(h lane) (a) and 1325 vehicles/(h lane) (b). Other model parameters are the same as those explained in Fig. 3.

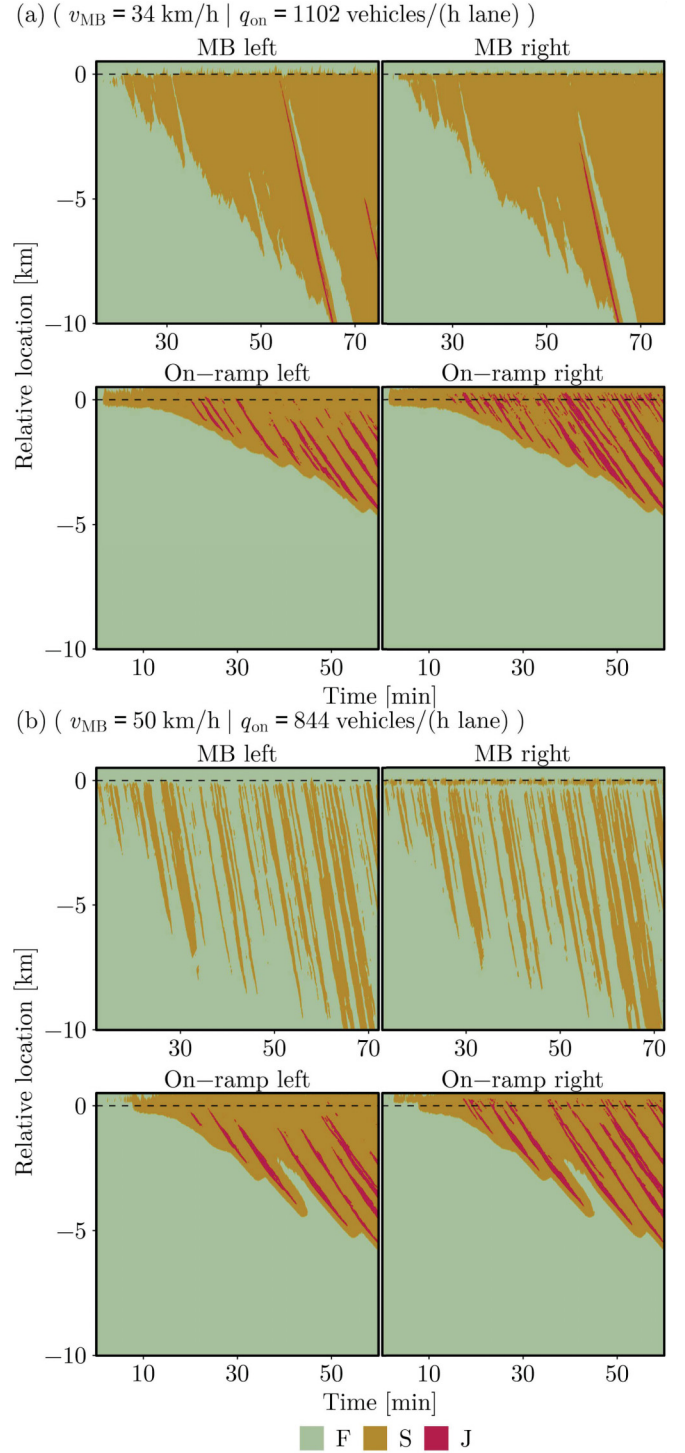


FIG. 7. Simulated traffic phases (F = free flow, S = synchronized flow, J = wide-moving jam) in time and space shown for the MB in the system coordinate moving at the velocity  $v_{MB}$  for different pairings ( $v_{MB} \mid q_{on}$ ). Panels (a) and (b) show two comparisons between MB and on ramp for the pairings ( $v_{MB} \mid q_{on}$ ) in Figs. 3(c) and 3(d). The flow rate  $q_{in}$  is chosen so that condition (2) is satisfied. The flow rate  $q_{in}$  is 1379 vehicles/(h lane) (a), and 1553 vehicles/(h lane) (b). Other model parameters are the same as those explained in Fig. 3.

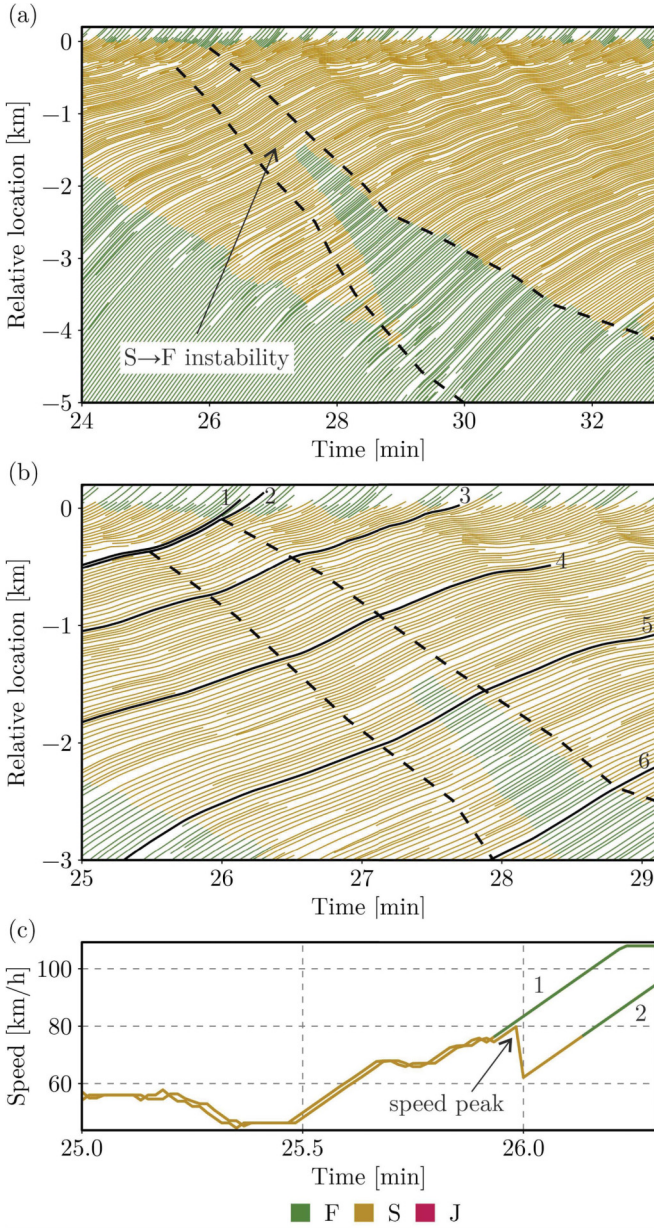


FIG. 8. Emergence of the  $S \rightarrow F$  transition at the MB shown in Fig. 5(c) through the occurrence of an  $S \rightarrow F$  instability. (a) Single-vehicle trajectories on the left lane around the  $S \rightarrow F$  transition. The bold dashed lines denote the development of the  $S \rightarrow F$  instability. (b) A further zoom-in on the trajectories from (a) with five marked trajectories through bold, black curves. The speed along the trajectories 1 and 2 in dependence of time is shown in (c). Vehicle 1 is moving on the left lane and has reached the downstream boundary of the synchronized flow. Therefore it is able to accelerate from the speed inside synchronized flow to the higher speed inside free flow. Vehicle 2, following vehicle 1, also starts to accelerate. However, a vehicle on the right lane uses the gap between vehicles 1 and 2 to change to the left lane, which forces vehicle 2 to decelerate, creating the speed peak. The color corresponds to the determined traffic phases (F = free flow, S = synchronized flow, J = wide-moving jam). Other model parameters are the same as those explained in Fig. 3.

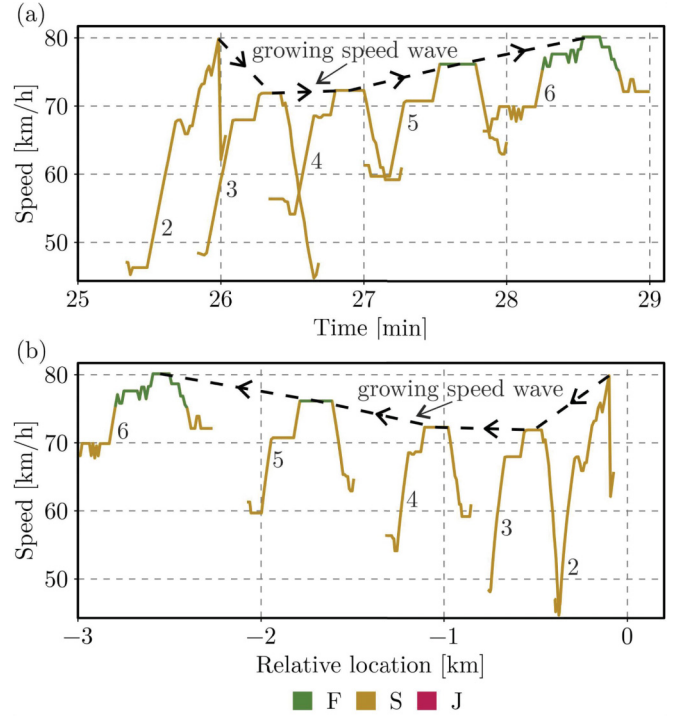


FIG. 9. Velocity along sections of the single vehicular trajectories 2–5 marked in Fig. 8(b). The speed (a) in dependence of time and (b) in dependence of relative location. The speed peak from Fig. 8(c) is the beginning of a speed wave of local speed increase within synchronized flow. While propagating further upstream, the amplitude and spatiotemporal extent of the speed wave increases, leading to an area of free flow inside synchronized flow. The color corresponds to the determined traffic phases (F = free flow, S = synchronized flow, J = wide-moving jam). Other model parameters are the same as those explained in Fig. 3.

instabilities inside the synchronized flow, using the method explained in Appendix D. We counted the number  $n_{SF}$  of realizations, where the  $S \rightarrow F$  instability occurred before the end of the observation time  $T_{ob}^{(cong)}$  and before the  $S \rightarrow J$  instability. This leads to following equation for probability  $P_{SF}$ :

$$P_{SF} = \frac{n_{SF}}{N_r^{(B)}}. \quad (6)$$

This probability  $P_{SF}$  of the  $S \rightarrow F$  instability was determined for each bottleneck and all pairings in Fig. 4. The influence of the simulation parameters  $q_{in}$ ,  $v_{MB}$ , and  $q_{on}$  on probability  $P_{SF}$  is shown in Fig. 10. For the MB, probability  $P_{SF}$  increases with higher velocities  $v_{MB}$  [Fig. 10(a)]. This corresponds to the observations made in examples beforehand, where a shift from GPs with no  $S \rightarrow F$  instability to MSPs with many  $S \rightarrow F$  instabilities can be seen (Fig. 5). In contrast, probability  $P_{SF}$  does not change with the increase in the flow rate  $q_{on}$  and no  $S \rightarrow F$  instabilities were observed at the on-ramp bottleneck. Hence, there are no  $S \rightarrow F$  transitions in the examples of the on-ramp bottleneck (Figs. 6 and 7). We do observe free flow inside the congested pattern at the

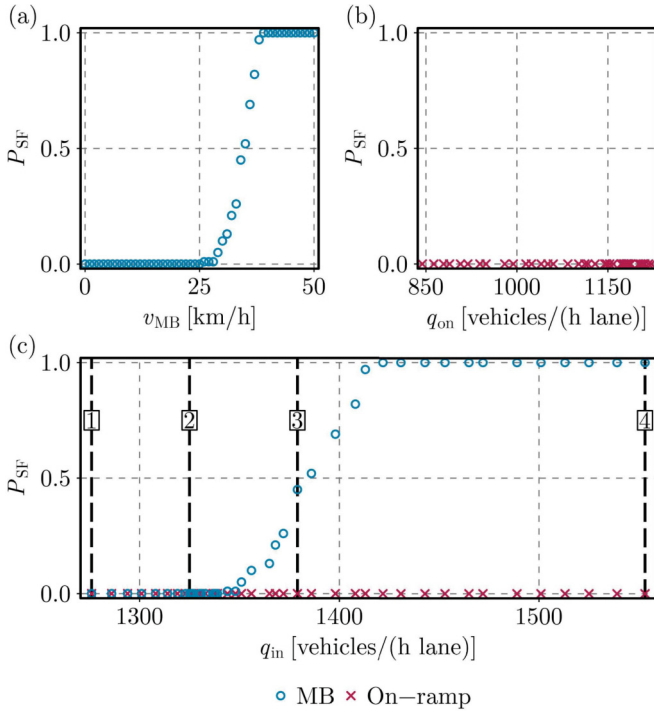


FIG. 10. Determined probability  $P_{SF}$  of an  $S \rightarrow F$  instability for MB against the velocity  $v_{MB}$  in (a) and for on ramp against the flow rate  $q_{on}$  in (b). A direct comparison between MB and on ramp can be made by plotting  $P_{SF}$  against the flow rate  $q_{in}$  on the main lanes, shown in (c). The vertical lines mark the examples from Figs. 6 and 7. Line 1 corresponds to (0 km/h | 1222 vehicles/(h lane)), 2 to (16 km/h | 1183 vehicles/(h lane)), 3 to (34 km/h | 1102 vehicles/(h lane)), and 4 to (50 km/h | 844 vehicles/(h lane)). The parameters  $q_{in}$ ,  $v_{MB}$  and  $q_{on}$  satisfy condition (2) (Fig. 4). The observation time after traffic breakdown is  $T_{ob}^{(cong)} = 60$  min. Other model parameters are the same as those explained in Fig. 3.

on-ramp bottleneck [Fig. 7(b)]; however, this is due to an  $S \rightarrow J \rightarrow S \rightarrow F$  transition, incited by an  $S \rightarrow J$  instability.

We can do a direct comparison of probability  $P_{SF}$  at the MB and on-ramp bottleneck by plotting the determined probabilities  $P_{SF}$  against the flow rate  $q_{in}$  on the main lanes, which is the same for each respective pairing [Fig. 10(c)]. This comparison shows the stark contrast between the MB and on-ramp bottleneck. While probability  $P_{SF}$  increases with rising flow rate  $q_{in}$  for the MB, it is unaltered for the on-ramp bottleneck.

### B. Explanation of the physics of $S \rightarrow F$ instability at moving bottleneck

The unique behavior of the MB can be explained through the movement of the bottleneck. Independent of the road bottleneck type, synchronized flow is usually fixed at the bottleneck [32]. Contrary to a road bottleneck, the downstream front of the synchronized flow is moving with the MB at the velocity  $v_{MB}$ , while the upstream front moves further upstream, independent of the movement of the downstream front of synchronized flow. This leads to a dilution of the

synchronized flow at the MB, respectively, distances between the vehicles inside the synchronized flow increase. With increase of the distances a smaller amplitude of a speed peak is necessary to be a nucleus for an  $S \rightarrow F$  instability. Therefore, the dilution of synchronized flow has an effect on the occurrence of the  $S \rightarrow F$  instability, which is proven further below.

This dilution of the synchronized flow can be revealed by examining distances  $g^{(S)}$  between vehicles inside synchronized flow. To minimize the influence of the upstream front of synchronized flow at the MB, where vehicles decelerate to the speed inside synchronized flow, only the distances  $g^{(S)}$  between vehicles, which are 500 m downstream of the upstream front, are considered. Furthermore only the distances  $g^{(S)}$  from the time of traffic breakdown at the MB until the occurrences of either  $S \rightarrow F$  or  $S \rightarrow J$  instabilities or until the end of the simulation are considered.

We already saw from the examples (Figs. 6 and 7) an obvious disparity in the synchronized flow formed at the MB with increasing velocity  $v_{MB}$  in comparison with the on-ramp bottleneck. The same observation can be made in the distribution of the distances  $g^{(S)}$  (Fig. 11). For the pairing (0 km/h | 1222 vehicles/(h lane)) the difference in the distributions for  $g^{(S)}$  at the MB and on-ramp bottleneck is small. Both distributions have a positive skew with an almost identical mean value. With decreasing flow rate  $q_{on}$  the distribution of the distances  $g^{(S)}$  for the on-ramp bottleneck does not change significantly. In contrast, the distribution of  $g^{(S)}$  in synchronized flow at the MB shows a strong dependency on the velocity  $v_{MB}$ . When the velocity  $v_{MB}$  increases, the distribution of  $g^{(S)}$  disperses and shifts to higher distances. This dispersion of the distances corresponds to the aforementioned dilution of the synchronized flow.

Although the mean values  $\bar{g}^{(S)}$  of the distances  $g^{(S)}$  are not able to describe the complex distributions as a whole, they still allow us an easier comparison of the pairings ( $v_{MB} | q_{on}$ ) (Fig. 12). The mean distance  $\bar{g}^{(S)}$  is increasing with the velocity  $v_{MB}$ , indicating the shift of the distributions to higher distances [Fig. 12(a)]. The slight decrease in the mean distance after the synchronized flow speed about 40 km/h is likely due to the method of filtering the relevant distances and can be ignored. In contrast to the MB, the mean distance  $\bar{g}^{(S)}$  for synchronized flow at the on-ramp bottleneck increases only slightly as the flow rate  $q_{on}$  decreases [Fig. 12(b)].

As beforehand, we can do a direct comparison of the pairings ( $v_{MB} | q_{on}$ ) by plotting the mean distance  $\bar{g}^{(S)}$  against the flow rate  $q_{in}$  on the main lanes [Fig. 12(c)]. A higher flow rate  $q_{in}$  corresponds to a higher velocity  $v_{MB}$  and a lower flow rate  $q_{on}$  on the on-ramp bottleneck, respectively. At lower flow rates  $q_{in}$  (e.g., pairing (0 km/h | 1222 vehicles/(h lane))) the difference in the mean distances  $\bar{g}^{(S)}$  for the MB and on-ramp bottleneck is small, explaining the similar congested patterns formed at the two different bottlenecks [Fig. 6(a)]. With increasing flow rate  $q_{in}$  the difference in the mean distances  $\bar{g}^{(S)}$  at the MB and on-ramp bottleneck increases, which is caused by the dilution of the synchronized flow at the MB. This leads to the different occurrences of the  $S \rightarrow F$  and  $S \rightarrow J$  instabilities inside the synchronized flow and, therefore, to the different congested patterns shown before (Figs. 6 and 7).

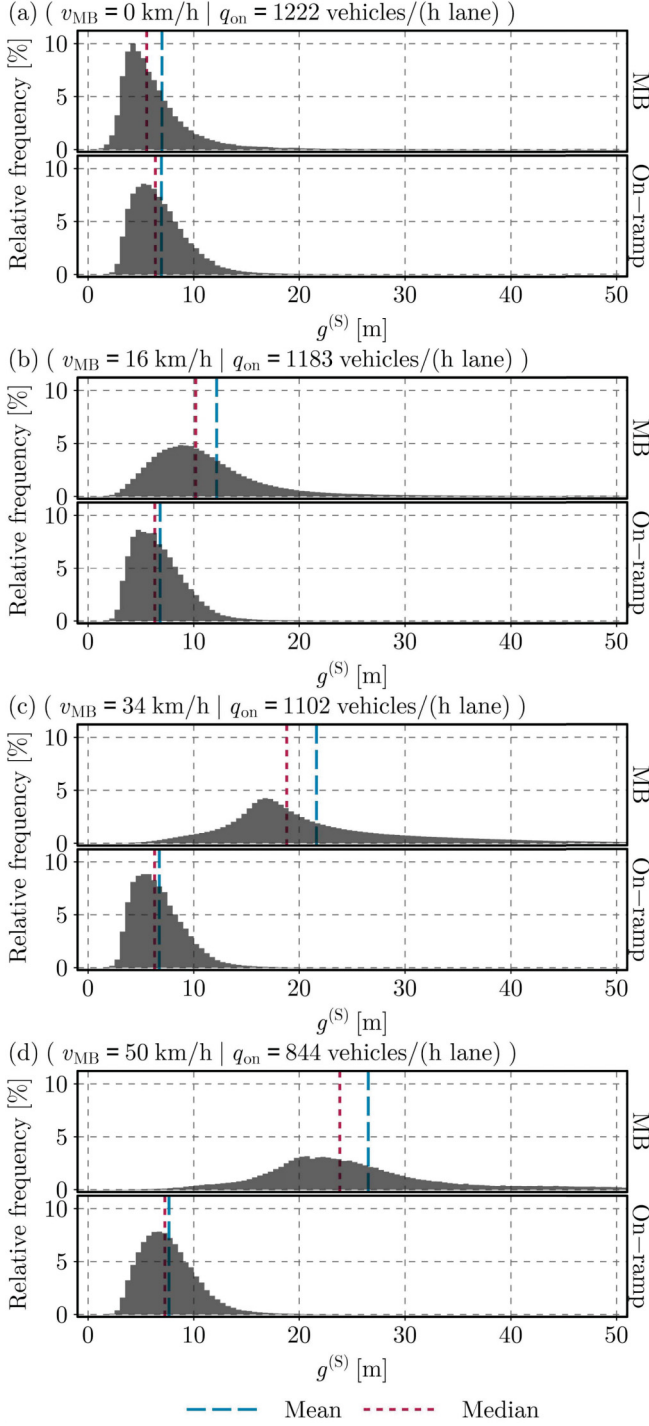


FIG. 11. Distribution of the space gap  $g^{(S)}$  in synchronized flow before an instability for the pairings  $(v_{MB} | q_{on})$  shown in Figs. 6 and 7. The histograms include all  $N_r^{(B)}$  realizations of the simulation, not only the ones shown in Figs. 6 and 7. The flow  $q_{in}$  on the main lanes is 1276 vehicles/(h lane) (a), 1325 vehicles/(h lane) (b), 1379 vehicles/(h lane) (c), and 1553 vehicles/(h lane) (d). For a better visualization the x axis is limited to 50 m. The blue, dashed line is the mean  $\bar{g}^{(S)}$  and the red, dotted line is the median of the space gap  $g^{(S)}$ . Other model parameters are the same as those explained in Fig. 3.

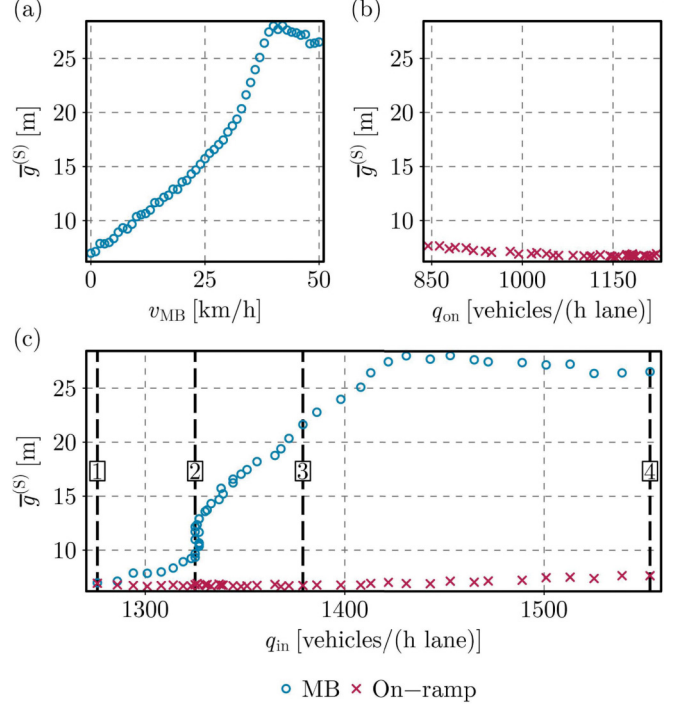


FIG. 12. The determined mean space gap  $\bar{g}^{(S)}$  in synchronized flow before an instability as a function of the velocity  $v_{MB}$  for an MB in (a) and of the flow rate  $q_{on}$  for an on ramp in (b). A direct comparison between MB and on ramp can be made by plotting  $\bar{g}^{(S)}$  against the flow rate  $q_{in}$  on the main lanes, shown in (c). The vertical lines mark the examples from Figs. 6 and 7. Line 1 corresponds to (0 km/h | 1222 vehicles/(h lane)), 2 to (16 km/h | 1183 vehicles/(h lane)), 3 to (34 km/h | 1102 vehicles/(h lane)), and 4 to (50 km/h | 844 vehicles/(h lane)). Other model parameters are the same as those explained in Fig. 3.

## V. PROBABILISTIC FEATURES OF SPATIOTEMPORAL COMPETITION BETWEEN $S \rightarrow F$ AND $S \rightarrow J$ INSTABILITIES IN SYNCHRONIZED FLOW AT MOVING BOTTLENECK

### A. $S \rightarrow J$ instability in synchronized flow at moving bottleneck

In addition to the  $S \rightarrow F$  instability, an  $S \rightarrow J$  instability in synchronized flow is possible [32]. The probability  $P_{SJ}$  for the appearance of the  $S \rightarrow J$  instability was determined, analogues to the probability  $P_{SF}$  of the  $S \rightarrow F$  instability in (6):

$$P_{SJ} = \frac{n_{SJ}}{N_r^{(B)}}, \quad (7)$$

with the number  $n_{SJ}$  of realizations, where the  $S \rightarrow J$  instability occurred before the end of the observation time  $T_{ob}^{(cong)}$  and before the  $S \rightarrow F$  instability occurred. The influence of the simulation parameters  $q_{in}$ ,  $v_{MB}$ , and  $q_{on}$  on probability  $P_{SJ}$  is shown in Fig. 13.

For the MB, probability  $P_{SJ}$  has a strong dependence on the velocity  $v_{MB}$  [Fig. 13(a)]. In contrast to the  $S \rightarrow F$  instability, the probability  $P_{SJ}$  of the  $S \rightarrow J$  instability decreases with higher velocities  $v_{MB}$ . Contrary to the MB, the flow rate  $q_{on}$

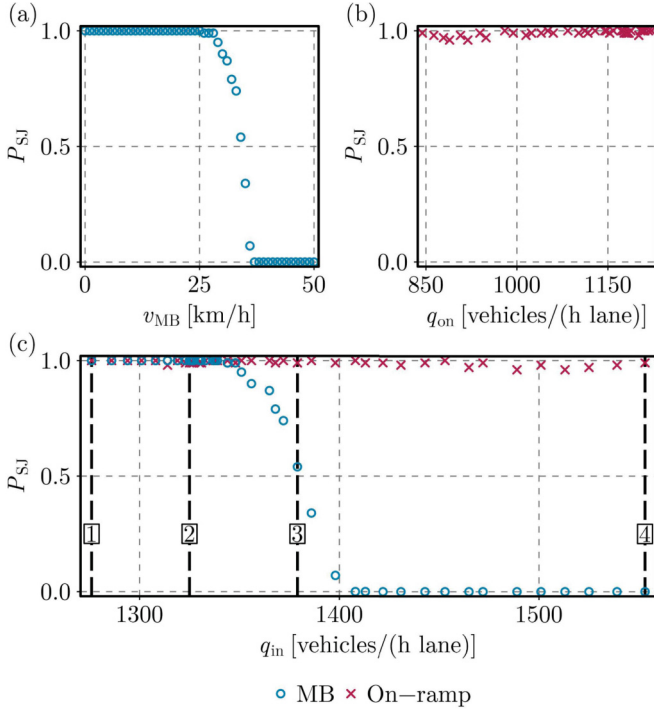


FIG. 13. Determined probability  $P_{SJ}$  of an  $S \rightarrow J$  instability for MB against the velocity  $v_{MB}$  (a) and for on-ramp bottleneck against the flow rate  $q_{on}$  (b). A direct comparison between MB and on-ramp bottleneck can be made by plotting  $P_{SJ}$  against the flow rate  $q_{in}$  on the main lanes (c). The vertical lines mark the examples from Figs. 6 and 7. Line 1 corresponds to (0 km/h | 1222 vehicles/(h lane)), 2 to (16 km/h | 1183 vehicles/(h lane)), 3 to (34 km/h | 1102 vehicles/(h lane)), and 4 to (50 km/h | 844 vehicles/(h lane)). The parameters  $q_{in}$ ,  $v_{MB}$  and  $q_{on}$  satisfy condition (2) (Fig. 4). The observation time after traffic breakdown is  $T_{ob}^{(cong)} = 60$  min. Other model parameters are the same as those explained in Fig. 3.

does not have a significant influence on probability  $P_{SJ}$  at the on-ramp bottleneck [Fig. 13(b)]. Probability  $P_{SJ}$  for the on-ramp bottleneck stays almost constant at the value 1, and it does not drop below 0.96. A direct comparison between the MB and on-ramp bottleneck is possible by plotting probabilities  $P_{SJ}$  against the flow rate  $q_{in}$  on the main lanes [Fig. 13(c)]. For small flow rates  $q_{in}$ , the probabilities  $P_{SJ}$  are equal to 1 for both the MB and on-ramp bottleneck. However, with rising  $q_{in}$ , probability  $P_{SJ}$  decreases for the MB, whereas it stays almost constant for the on-ramp bottleneck.

The influence or lack thereof of the simulation parameters  $q_{in}$ ,  $v_{MB}$  and  $q_{on}$  on probabilities  $P_{SF}$  and  $P_{SJ}$  of the  $S \rightarrow F$  and  $S \rightarrow J$  instabilities (Figs. 10 and 13) explains the difference between the MB and on-ramp bottleneck (Figs. 6 and 7). For the pairings (0 km/h | 1222 vehicles/(h lane)) and (16 km/h | 1183 vehicles/(h lane)) we determined almost identical values of the probabilities  $P_{SF}$  and  $P_{SJ}$  for the MB and on-ramp bottleneck. Therefore, both pairings show GPs, at the two different bottlenecks. However, there is a difference in the GPs for pairing (16 km/h | 1183 vehicles/(h lane)). At the MB we have multiple  $S \rightarrow J \rightarrow S \rightarrow F$  transitions, not observed at the on-ramp bottleneck. The larger distances  $g^{(S)}$

between the vehicles inside synchronized flow at the MB [Fig. 11(b)] can explain why  $S \rightarrow J$  instabilities lead more often to  $S \rightarrow J \rightarrow S \rightarrow F$  transitions at the MB than at the on-ramp bottleneck.

Pairing (34 km/h | 1102 vehicles/(h lane)) is the first example where the probabilities  $P_{SF}$  and  $P_{SJ}$  are different for the MB and on-ramp bottleneck. At the MB we first observe an WSP, which is interrupted by an  $S \rightarrow F$  instability and then followed by an GP. This corresponds to the determined probabilities  $P_{SF}$  and  $P_{SJ}$ , which are both larger than 0 at the MB. The probabilities  $P_{SF}$  and  $P_{SJ}$  do not change for the on-ramp bottleneck, therefore, we once again observe an GP. For the pairing (50 km/h | 844 vehicles/(h lane)) the difference of the observed congested patterns at both bottlenecks is explained by the difference in the probabilities  $P_{SF}$  and  $P_{SJ}$ , which is largest for this pair. Although we have an GP at the on-ramp bottleneck, we observe an  $S \rightarrow J \rightarrow S \rightarrow F$  transition. For the flow rate  $q_{on} = 844$  vehicles/(h lane) at the on-ramp bottleneck, the distances  $g^{(S)}$  inside synchronized flow are larger than for the other examples [Figs. 11 and 12(b)]. This supports the hypothesis made beforehand that larger distances inside synchronized flow encourage the development of an  $S \rightarrow J \rightarrow S \rightarrow F$  transition from the  $S \rightarrow J$  instability. This will not be examined further in this paper, but could be a topic of interest for future research.

### B. $S \rightarrow F$ and $S \rightarrow J$ instabilities at moving bottleneck

There can be a competition between the  $S \rightarrow F$  and  $S \rightarrow J$  instabilities in synchronized flow [36]. We have found the following three possible outcomes of this competition in synchronized flow at the MB: The appearance of an  $S \rightarrow F$  instability, the appearance of an  $S \rightarrow J$  instability or the persisting of synchronized flow without an instability. For the last possibility, that the synchronized flow is uninterrupted and persists at the bottleneck, exists the probability  $P_S$ :

$$P_S = \frac{n_S}{N_r^{(B)}}, \quad (8)$$

with the number  $n_S$  of realizations, where there are no instabilities during the observation time  $T_{ob}^{(cong)} = 60$  min after traffic breakdown. Naturally, the three probabilities  $P_{SF}$ ,  $P_{SJ}$ , and  $P_S$  are connected by following relation:

$$P_{SF} + P_{SJ} + P_S = 1. \quad (9)$$

The competition between the  $S \rightarrow F$  and  $S \rightarrow J$  instabilities is represented by a nonzero probability  $P_S$  of uninterrupted synchronized flow in which no  $S \rightarrow F$  and no  $S \rightarrow J$  instability occurs during the observation time  $T_{ob}^{(cong)}$ . By combining the previous result for the probability  $P_{SF}$  at the MB [Fig. 10(a)] with the result for the probability  $P_{SJ}$  at the MB [Fig. 13(a)] using (9), we reveal the competition between the  $S \rightarrow F$  and  $S \rightarrow J$  instabilities at the MB (Fig. 14). The probability  $P_S$  for the MB is not zero, changes with the velocity  $v_{MB}$  and has a global maximum. For the MB, the determined probabilities  $P_{SF}$  and  $P_{SJ}$  in dependence of the velocity  $v_{MB}$  can be fitted by the following functions  $\tilde{P}_{SF}$  and  $\tilde{P}_{SJ}$ :

$$\begin{aligned} \tilde{P}_{SF}(v_{MB}) &= (1 + e^{-\beta_{SF}(v_{MB} - v_{p,SF})})^{-1}, \\ \tilde{P}_{SJ}(v_{MB}) &= (1 + e^{\beta_{SJ}(v_{MB} - v_{p,SJ})})^{-1}, \end{aligned} \quad (10)$$

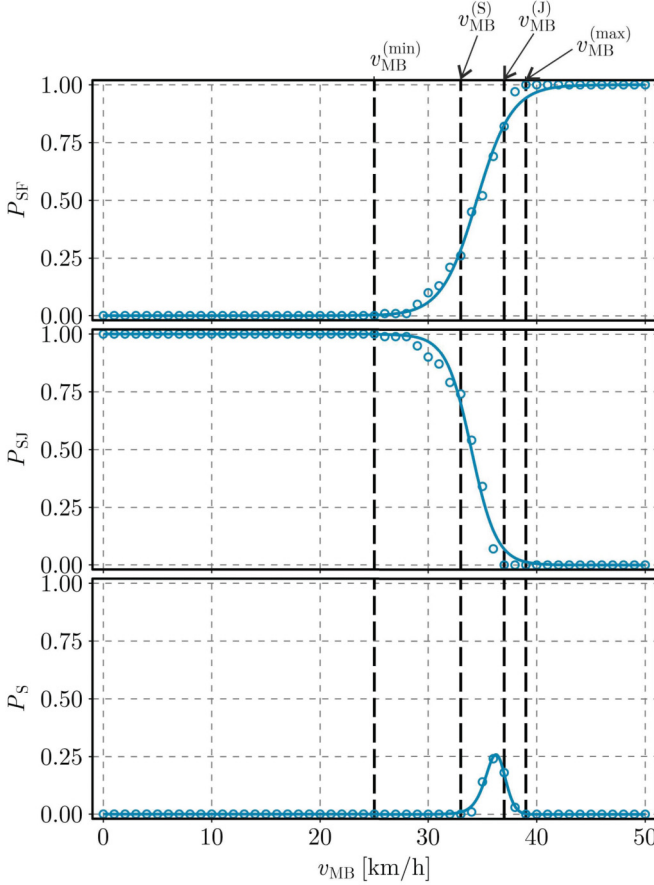


FIG. 14. Determined probability of an  $S \rightarrow F$  instability  $P_{SF}$ , of an  $S \rightarrow J$  instability  $P_{SJ}$ , and of uninterrupted synchronized flow  $P_S$  for the MB against the velocity  $v_{MB}$ . Characteristic parameters are  $v_{MB}^{(min)} = 25$  km/h,  $v_{MB}^{(S)} = 33$  km/h,  $v_{MB}^{(J)} = 37$  km/h, and  $v_{MB}^{(max)} = 39$  km/h. The parameters  $q_{in}$ ,  $v_{MB}$ , and  $q_{on}$  satisfy condition 2 (Fig. 4). The observation time after traffic breakdown is  $T_{ob}^{(cong)} = 60$  min. Other model parameters are the same as those explained in Fig. 3.

where  $\beta_{SF}$ ,  $v_{p,SF}$ ,  $\beta_{SJ}$ , and  $v_{p,SJ}$  are fit parameters. From (9) and (10) follows also a fit for probability  $P_S$  of uninterrupted synchronized flow. All three fits are shown together with the corresponding simulation results in Fig. 14.

We have shown, that the mean distance  $\bar{g}^{(S)}$  inside synchronized flow at the MB has a strong dependence on the velocity  $v_{MB}$  (Fig. 12). The same is true for the probabilities  $P_{SF}$  and  $P_{SJ}$  of the  $S \rightarrow F$  and  $S \rightarrow J$  instabilities (Fig. 14). An opportunity arises to combine these two observations and show the dependency of the probabilities  $P_{SF}$ ,  $P_{SJ}$ , and  $P_S$  on the mean distance  $\bar{g}^{(S)}$  inside synchronized flow (Fig. 15).

For the MB, probability  $P_{SF}$  of the  $S \rightarrow F$  instability increases with higher mean distances  $\bar{g}^{(S)}$ , while probability  $P_{SJ}$  of the  $S \rightarrow J$  instability decreases. This proves that the aforementioned dilution of the synchronized flow at the MB is responsible for the difference in the probabilities  $P_{SF}$  and  $P_{SJ}$  and, therefore, responsible for the difference in congested patterns at the MB and on-ramp bottleneck (Figs. 6 and 7).

The determined probabilities  $P_{SF}$  and  $P_{SJ}$  in dependence of the mean space gap  $\bar{g}^{(S)}$  can be fitted by following functions

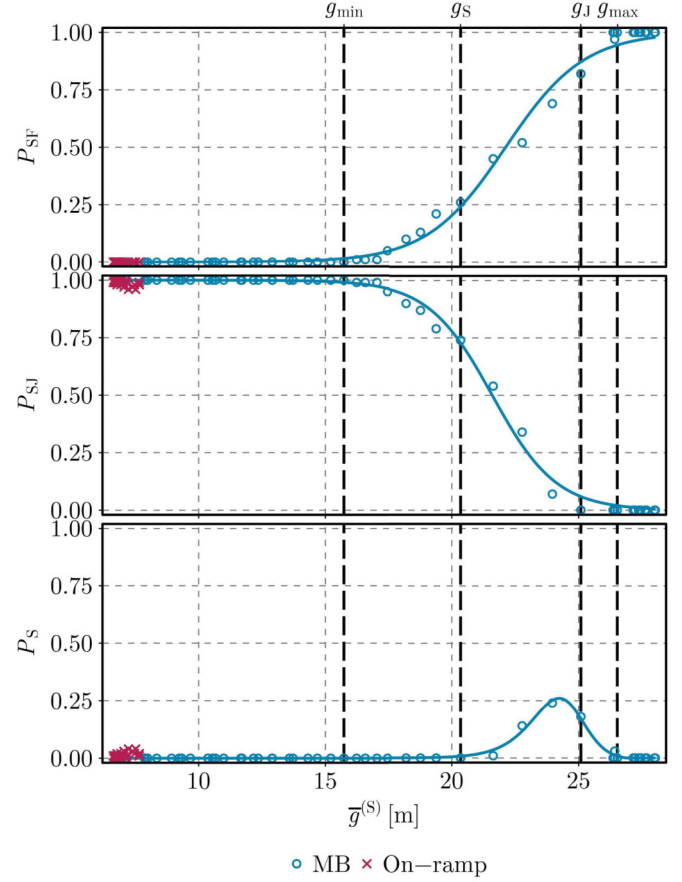


FIG. 15. Determined probability of an  $S \rightarrow F$  instability  $P_{SF}$ , of an  $S \rightarrow J$  instability  $P_{SJ}$  and of uninterrupted, synchronized flow  $P_S$  for the MB and on-ramp bottleneck against the mean space gap  $\bar{g}^{(S)}$ . Characteristic parameters are  $g_{min} = 15.7$  m,  $g_S = 20.3$  m,  $g_J = 25.1$  m, and  $g_{max} = 26.5$  m. The parameters  $q_{in}$ ,  $v_{MB}$ , and  $q_{on}$  satisfy condition 2 (Fig. 4). The observation time after traffic breakdown is  $T_{ob}^{(cong)} = 60$  min. Other model parameters are the same as those explained in Fig. 3.

$\tilde{P}_{SF}$  and  $\tilde{P}_{SJ}$ :

$$\begin{aligned} \tilde{P}_{SF}(\bar{g}^{(S)}) &= (1 + e^{-\gamma_{SF}(\bar{g}^{(S)} - g_{p,SF})})^{-1}, \\ \tilde{P}_{SJ}(\bar{g}^{(S)}) &= (1 + e^{\gamma_{SJ}(\bar{g}^{(S)} - g_{p,SJ})})^{-1}, \end{aligned} \quad (11)$$

where  $\gamma_{SF}$ ,  $g_{p,SF}$ ,  $\gamma_{SJ}$ , and  $g_{p,SJ}$  are fit parameters. From (9) and (11) follows also a fit for probability  $P_S$  of uninterrupted, synchronized flow. All three fits are shown together with the corresponding simulation results in Fig. 15.

There are four characteristic values of the velocity  $v_{MB}$ :  $v_{MB}^{(min)}$ ,  $v_{MB}^{(S)}$ ,  $v_{MB}^{(J)}$ , and  $v_{MB}^{(max)}$ , or, respectively, for the mean space gap  $\bar{g}^{(S)}$ :  $g_{min}$ ,  $g_S$ ,  $g_J$ , and  $g_{max}$  (Figs. 14 and 15). These values define intervals of the velocity  $v_{MB}$  or the mean space gap  $\bar{g}^{(S)}$ , respectively, where the probabilities  $P_{SF}$ ,  $P_{SJ}$ , and  $P_S$  show a certain behavior:

$$\begin{aligned} P_S \in (0, 1) & \quad \text{for} \quad v_{MB} \in (v_{MB}^{(S)}, v_{MB}^{(max)}) \vee \\ & \quad \bar{g}^{(S)} \in (g_S, g_{max}), \\ P_S = 0 & \quad \text{for} \quad v_{MB} \notin (v_{MB}^{(S)}, v_{MB}^{(max)}) \vee \\ & \quad \bar{g}^{(S)} \notin (g_S, g_{max}), \end{aligned}$$

$$\begin{aligned}
P_{SF} \in (0, 1) \quad & \text{for } v_{MB} \in (v_{MB}^{(\min)}, v_{MB}^{(J)}) \vee \\
& \bar{g}^{(S)} \in (g_{\min}, g_J), \\
P_{SJ} \in (0, 1) \quad & \text{for } v_{MB} \in (v_{MB}^{(\min)}, v_{MB}^{(J)}) \vee \\
& \bar{g}^{(S)} \in (g_{\min}, g_J). \quad (12)
\end{aligned}$$

The results show that there is an interval  $(v_{MB}^{(S)}, v_{MB}^{(J)})$  or  $(g_S, g_J)$ , respectively, where all three probabilities  $P_{SF}$ ,  $P_{SJ}$ , and  $P_S$  are larger than 0 (Figs. 14 and 15). This means that for identical simulation parameters  $q_{in}$  and  $v_{MB}$  but different realizations, it is possible to either observe an  $S \rightarrow F$  instability, an  $S \rightarrow J$  instability or no instability case. An example of this phenomenon is shown for the velocity of the MB  $v_{MB} = 36$  km/h, where probability  $P_S$  of uninterrupted synchronized flow has its maximum (Fig. 16). The first realization is interrupted by an  $S \rightarrow F$  instability, whereas the second one has an  $S \rightarrow J$  instability leading to an  $S \rightarrow J \rightarrow S \rightarrow F$  transition. Uninterrupted synchronized flow without any instability is observed in the third realization.

## VI. DISCUSSION

### A. Evaluations of stochastic traffic flow model based on empirical data

The Kerner-Klenov stochastic microscopic model (Appendix A) has been used in all simulations made in this paper. However, a question can arise whether reliable validations and parameter calibration of this model with the use of real field data have been made. It should be noted that microscopic empirical traffic data for a study of traffic breakdown at MBs and, therefore, for some empirical study of the  $S \rightarrow F$  instability at the MBs are currently not available. We know only one empirical example of a complex congested pattern observed at an MB in paper [91], in which traffic breakdown features have not been studied. However, there are a number of empirical microscopic data for a study of traffic breakdown and other phase transitions at on- and off-ramp bottlenecks (see references in [33]).

In 2003 the Kerner-Klenov model was validated and calibrated based on a huge number of spatiotemporal traffic data measured at different highways during 1996–2001. Later, special empirical validations of the model have been made based on real field data measured on multilane highways during 2002–2006 [92,93].

In 2013 the stochastic microscopic model was calibrated based on TomTom empirical probe vehicle data [35]. In particular, it has been found that lane changing rules and models for vehicle merging at bottlenecks used in the Kerner-Klenov model that has been expanded for a three-lane road scenario can simulate traffic breakdown ( $F \rightarrow S$  transition) at bottlenecks and resulting congested patterns relate very closely with those found in empirical data measured on three-lane highway sections with bottlenecks [32,35].

Simulations of city traffic with the model used in the paper [94] have predicted a possible dissolution of vehicle queues at traffic signal (so-called jam absorption effect) with the subsequent formation of synchronized flow. These simulation results have been confirmed in empirical studies of city traffic [95].

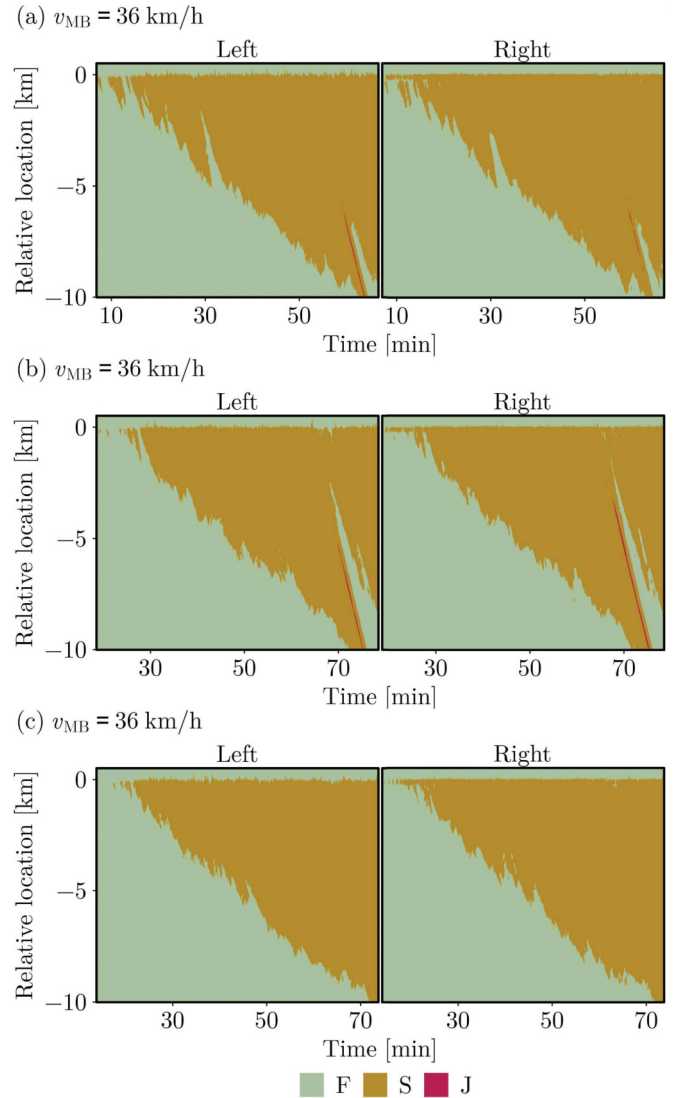


FIG. 16. Simulated traffic phases (F = free flow, S = synchronized flow, J = wide-moving jam) in time and space shown in system coordinate moving at the velocity  $v_{MB}$  for different realizations of identical simulation parameters. In (a) the synchronized flow is interrupted by an  $S \rightarrow F$  instability, in (b) by an  $S \rightarrow J$  instability, and in (c) there is no instability. The velocity of the MB is  $v_{MB} = 36$  km/h, which corresponds to mean space gap  $\bar{g}^{(S)} = 24.0$  m and the maximum of probability  $P_S$  (Figs. 14 and 15). Probabilities are  $P_{SF} = 0.69$ ,  $P_{SJ} = 0.07$ , and  $P_S = 0.24$ . The flow rate  $q_{in}$  is 1398 vehicles/(h lane). Other model parameters are the same as those explained in Fig. 3.

With the use of this model it was predicted [96] that moving synchronized flow patterns (MSPs) can occur at traffic signal in city traffic. Empirical MSPs have been indeed observed through the use of aerial traffic observations (with the use of a drone) by Kaufmann *et al.* [97].

With the use of the model, Kerner [34] predicted sequences of  $F \rightarrow S \rightarrow F$  transitions before traffic breakdown at bottlenecks. The sequences have been indeed observed in recent empirical studies of probe vehicle data [98].

Empirical moving jams often observed in empirical data of congested traffic are also called “speed oscillations” or

“traffic oscillations” in congested traffic (see, e.g., reviews [13,14] and references in [99,100]). In some empirical studies, the growth of traffic oscillations leads to the emergence of a wide-moving jam(s) ( $S \rightarrow J$  transition). However, in some other empirical studies, the growth of traffic oscillations is interrupted over time. Therefore, it also exists empirical data in which traffic oscillations do not necessarily grow into wide-moving jams (see examples of such empirical results in [30]). In car-following experiments and empirical studies, Jiang *et al.* [99] have found that the growth of traffic oscillations occurs in a concave way. The concave growth of traffic oscillations can also be simulated by the Kerner-Klenov model (Fig. 17).

### B. Explanations of crucial difference between Kerner’s $S \rightarrow F$ instability and classical traffic instability

In the microscopic stochastic model [37,39–41,88] used in all simulations, there can be two qualitatively different instabilities in synchronized flow of the three-phase traffic theory [33]: an  $S \rightarrow F$  instability or an  $S \rightarrow J$  instability.

The  $S \rightarrow F$  instability results from a discontinuous character of over-acceleration together with a spatiotemporal competition between over-acceleration and speed adaptation (see explanations in Chap. 8 of [33]). In turn, the discontinuous character of over-acceleration is caused by a finite value of the mean time in over-acceleration. The  $S \rightarrow F$  instability is caused by the time delay in over-acceleration. The discontinuous character of the mean time delay in over-acceleration is responsible for the nucleation nature of traffic breakdown ( $F \rightarrow S$  transition) at a bottleneck. In other words, the competition between the  $S \rightarrow F$  instability and speed adaptation governs the nucleation nature of the  $F \rightarrow S$  transition at the bottleneck. The  $S \rightarrow F$  instability is a growth of a local speed *increase* in synchronized flow.

The local speed increase in synchronized flow, that can initiate Kerner’s  $S \rightarrow F$  instability at a bottleneck, has been called in [34] a “speed peak” in synchronized flow. An example of the speed peak in synchronized flow at the MB is shown in Fig. 8(c). In Sec. 5.12 of [32], a detailed explanation of the mechanism of the occurrence of the speed peak in synchronized flow at a bottleneck has been made.<sup>2</sup> It should be emphasized that there can also be other mechanisms of the

<sup>2</sup>In Fig. 5.25 of [32] as well as in Fig. 8(c) of the paper, it can be seen that the speed peak occurs at the downstream front of synchronized flow at the bottleneck: The acceleration of a vehicle [vehicle 2 in Fig. 5.25 of [32] and vehicle 2 in Fig. 8(c)] from synchronized flow to free flow at the downstream front of synchronized flow is interrupted through a slow-moving vehicle that merges ahead of the vehicle. As a result, the vehicle [vehicle 2 in Fig. 5.25 of [32] and vehicle 2 in Fig. 8(c)] must decelerate. Thus, the merging of the slow vehicle ahead of the initial accelerating vehicle causes the occurrence of the speed peak (local speed increase) at the downstream front of synchronized flow. There is a difference between the occurrence of the speed peak at the downstream front of synchronized flow at the on-ramp bottleneck considered in [32,34] and at the MB studied in this paper that is as follows. At the on-ramp bottleneck, a slow-moving vehicle that causes the occurrence of the speed peak merges from the on-ramp lane of the bottleneck onto the main road. At the

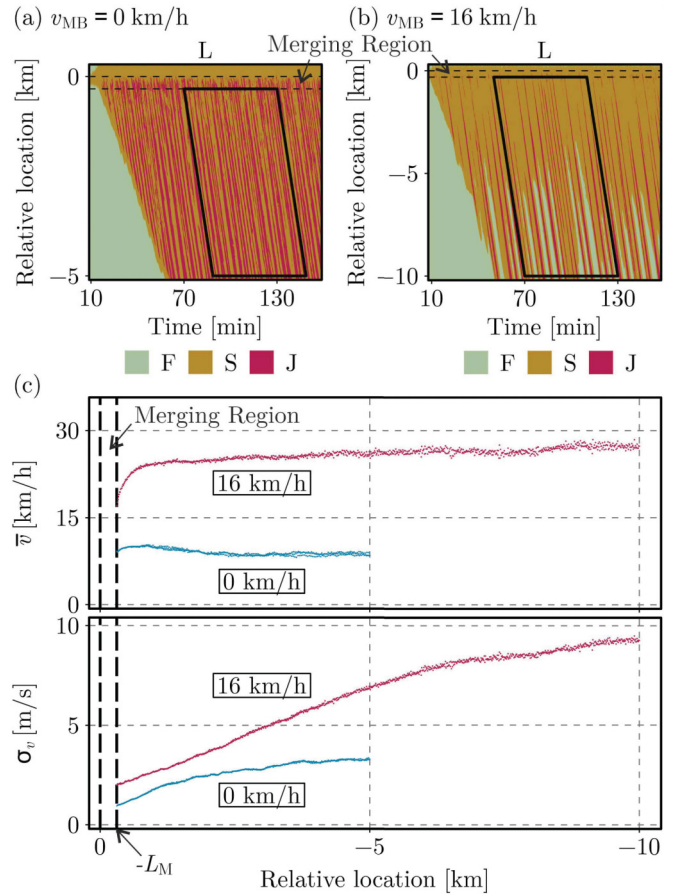


FIG. 17. Simulations of the concave growth of traffic oscillations of Jiang *et al.* with the Kerner-Klenov model. Panels (a) and (b) show a continuation from Fig. 6 of the simulated traffic phases ( $F$  = free flow,  $S$  = synchronized flow,  $J$  = wide-moving jam) in time and space for the MB in system coordinates moving at the velocity  $v_{MB}$  on the left main lane. The parallelogram-shaped region with a width of 60 min marks the data used for the analyses in (c). By dividing this region in cells of length 10 m and averaging inside these cells and over the time, we calculated in (c) the mean speed  $\bar{v}$  and the corresponding standard deviation  $\sigma_v$  that exhibits the concave growth. This method was used in [100] to show concave growth in speed of Jiang *et al.* in experimental data. The standard deviation  $\sigma_v$  is shown only upstream of the merging region  $L_M = 300$  m [Fig. 2(a)] to focus on the concave growth. In (a) and (b), the moving jams (traffic oscillations) emerge through the classical traffic instability ( $S \rightarrow J$  instability) that occur in synchronized flow at the MB with probability  $P_{SJ} = 1$ , whereas the Kerner’s  $S \rightarrow F$  instability does not occur (probability  $P_{SF} = 0$ ) for  $v_{MB} = 0$  km/h and  $v_{MB} = 16$  km/h (Fig. 14). The flow rate  $q_{in}$  is 1276 vehicles/(h lane) in (a), 1325 vehicles/(h lane) in (b). Other model parameters are the same as those explained in Fig. 3.

MB, a slow-moving vehicle that causes the occurrence of the speed peak at the downstream front of synchronized flow changes from the right lane [in which the MB moves, Fig. 2(a)] to the left lane [see explanations in caption to Fig. 8(c)].

occurrence of a local speed increase in synchronized flow that can initiate the development of Kerner's  $S \rightarrow F$  instability.<sup>3</sup>

Contrary to the  $S \rightarrow F$  instability, the  $S \rightarrow J$  instability is caused by the well-known driver reaction time (driver over-reaction). The  $S \rightarrow J$  instability is responsible for the emergence and growth of the moving jams (growth of traffic oscillations). The  $S \rightarrow J$  instability is a growth of a local speed *decrease* in synchronized flow. In other words, the  $S \rightarrow J$  instability is the well-known classical traffic flow instability. The term " $S \rightarrow J$  instability" for the classical traffic instability has been introduced in the three-phase traffic theory to distinguish the classical traffic instability incorporated in standard traffic models from the  $S \rightarrow F$  instability incorporated in the microscopic model used in this paper.

As postulated in the three-phase traffic theory, the time delay in over-acceleration should not necessarily depend on the existence of the driver reaction time. Even if the driver reaction time were negligibly short, the mean time delay in over-acceleration is a finite value. The driver reaction time is responsible for the classical traffic instability ( $S \rightarrow J$  instability) in synchronized flow, *not* for traffic breakdown ( $F \rightarrow S$  transition) in free flow at the bottleneck. Traffic breakdown ( $F \rightarrow S$  transition) in free flow at the bottleneck is associated with the time delay in over-acceleration, *not* with the driver reaction time.

It should be mentioned that in the models, in which traffic breakdown is explained by the classical traffic instability (e.g., [12–14,16–26,99–102]), the growth of traffic oscillations can lead to the emergence of free flow between the growing moving jams. In these models, the occurrence of free flow between traffic oscillations has *no relation* to the  $S \rightarrow F$  instability of the three-phase traffic theory. Indeed, in this case free flow results from the growth of traffic oscillations. Contrary to the models, in which traffic breakdown is explained by the classical traffic instability (e.g., [12–14,16–26,99–102]), in the Kerner-Klenov model the occurrence of the  $S \rightarrow F$  transition can be realized *without* the occurrence of the growing traffic oscillations. This is because the model incorporates both the  $S \rightarrow J$  instability leading to growth of traffic oscillations (wave of local speed decrease) and the  $S \rightarrow F$  instability leading to the growth of waves of local speed increase. Therefore, these two instabilities can occur independent of each other.

This conclusion is illustrated in Fig. 14: Contrary to the classical traffic instability ( $S \rightarrow J$  instability) leading to the growth of traffic oscillations, in our paper at a large enough

velocity of the MB ( $v_{MB} \geq 37$  km/h; Fig. 14) the probability  $P_{SJ}$  of the  $S \rightarrow J$  instability is equal to zero: No growth of traffic oscillations can occur. Rather than the growth of traffic oscillations (i.e., the growth of waves of local speed *decrease* in synchronized flow), the growth of speed waves of local speed *increase* is realized in synchronized flow, i.e., the  $S \rightarrow F$  instability does occur. Indeed, at large enough velocities of the MB ( $v_{MB} \geq 39$  km/h; Fig. 14), the probability  $P_{SF}$  of the  $S \rightarrow F$  instability is equal to 1.

Thus, the  $S \rightarrow F$  instability is a growth of a local speed *increase* in synchronized flow. Contrary to the  $S \rightarrow F$  instability, the  $S \rightarrow J$  instability is a growth of a local speed *decrease* in synchronized flow. However, traffic flow models that do not incorporate the discontinuous character of over-acceleration of the three-phase traffic theory like all traffic models in which traffic breakdown at a bottleneck is explained by the development of the classical traffic flow instability (see, e.g., references to such models in reviews [12–14,16–24] and papers [99–102]) have not shown the nucleation nature of the  $S \rightarrow F$  instability and the associated competition between the  $S \rightarrow F$  and  $S \rightarrow J$  instability studied in our paper (Fig. 14).

### C. Differences with previous studies of moving bottleneck in the framework of three-phase traffic theory

In [88], in which a study of traffic phenomena at an MB in the framework of three-phase traffic theory has been made, the traffic phenomena including phase transitions as those in this paper under consideration have been studied.

However, in [88] it was still not known that an  $S \rightarrow F$  transition is caused by an  $S \rightarrow F$  instability that exhibits the nucleation nature; in its turn, the nucleation nature of the  $S \rightarrow F$  instability governs the nucleation nature of the  $F \rightarrow S$  transition at a bottleneck [34]. A possibility of a competition between the  $S \rightarrow F$  and  $S \rightarrow J$  instabilities has also still not been known [36]. In this paper, we revealed that there is a basic physical difference between statistical features of synchronized flow at the on-ramp bottleneck studied in [34,36] and at the MB studied here:

(1) The motion of the downstream front of synchronized flow at the MB causes a *dilution* of synchronized flow at the MB [Fig. 12(a)].

(2) The dilution of synchronized flow at the MB results in the considerable increase in probability of the occurrence of the  $S \rightarrow F$  instability at the MB (Figs. 14 and 15).

(3) In contrast to the MB, such a dilution of synchronized flow does not occur at the on-ramp bottleneck [Fig. 12(b)].

(4) At the same probability of traffic breakdown ( $F \rightarrow S$  transition) at the MB and the on-ramp bottleneck, contrary to the MB, *no*  $S \rightarrow F$  instability is realized in synchronized flow at the on-ramp bottleneck [Fig. 10(b)].

(5) The dilution of the synchronized flow at the MB causes different statistical behavior of synchronized flow at the MB in comparison with the on-ramp bottleneck (Fig. 15).

This crucial qualitative difference in the behavior of the statistical features of synchronized flow at the MB with the on-ramp bottleneck revealed in this paper can be explained by the fact that for all road bottlenecks (on- and off-ramp bottlenecks as well as merge bottleneck, etc.) the downstream front of synchronized flow is fixed at the stationary location

<sup>3</sup>In particular, through the over-acceleration effect, a local speed increase can spontaneously occur in a car-following platoon moving at the synchronized flow speed; if the local speed increase is large enough, Kerner's  $S \rightarrow F$  instability is realized. Simulations of the occurrence of the local speed increase and the  $S \rightarrow F$  instability in a car-following platoon in synchronized flow, in which all vehicles move initially at the same mean speed, have been presented in Sec. 5.11 of [32]. Simulations show that the local speed increase should not necessarily be accompanied by a local speed decrease [see Fig. 5.22(b) of [32]]. Different physical mechanisms of the over-acceleration effect that can cause a local speed increase in synchronized flow with the subsequent development of the  $S \rightarrow F$  instability have been considered in Sec. 5.10 of [32].

of the road bottleneck. Contrarily, the downstream front of synchronized flow at the MB is moving with the velocity  $v_{\text{MB}}$ . The motion of the downstream front of synchronized flow causes the dilution of synchronized flow at the MB. The mean space gap  $\bar{g}^{(S)}$  between the vehicles inside synchronized flow is linked to the velocity  $v_{\text{MB}}$  of the MB (Fig. 12). An increase in the velocity  $v_{\text{MB}}$  leads to a stronger dilution of synchronized flow, hence to an increase in the mean space gap  $\bar{g}^{(S)}$ . In contrast, the on-ramp bottleneck is a road bottleneck. Contrary to the MB, at a given probability  $P_{\text{FS}}^{(B)}$  of traffic breakdown (F  $\rightarrow$  S transition) at the on-ramp bottleneck the flow rate  $q_{\text{on}}$  does not have a significant influence on the mean space gap  $\bar{g}^{(S)}$  in synchronized flow. Therefore, while we observe the dilution of synchronized flow at the MB, we do not observe the same effect at the on-ramp bottleneck.

#### D. Traffic characteristics for comparison of MB and on-ramp bottleneck: Bottlenecks strengths

In all empirical observations (e.g., [13–15,17–19,21,22,30–33]), the onset of traffic congestion occurs at a bottleneck. This is because the bottleneck introduces a speed decrease localized at the bottleneck (local speed decrease, for short). Traffic breakdown is the F  $\rightarrow$  S transition that exhibits the empirical nucleation nature [30–33]. In most empirical observations (see Chaps. 4 and 9 of [33]), the local speed decrease at a bottleneck plays the role of a nucleus for the occurrence of traffic breakdown at the bottleneck (F  $\rightarrow$  S transition). This explains both why traffic breakdown occurs mostly at the bottleneck and why the value of the local speed decrease plays the decisive role in the nucleation of the F  $\rightarrow$  S transition at the bottleneck.

A local speed decrease at the on-ramp bottleneck is caused by the deceleration of vehicles moving on the main lane due to slower vehicles merging from the on-ramp lane onto the main lane. A local speed decrease at the MB is caused by the lane changing of vehicles in the merging region of the MB moving in the right lane (Sec. A 5 of Appendix A): Vehicles that move in the right lane change to the left lane to pass the MB; this lane changing causes the deceleration of vehicles in the left lane provoking the occurring of the local speed disturbance (a more detailed explanation of the physics of the local speed decrease at the MB and on-ramp bottleneck can be found in Chap. 4 of [33]).

Thus, at a given flow rate on the main lane  $q_{\text{in}}$ , the larger the on-ramp flow rate  $q_{\text{on}}$  is, the larger is on average the local speed decrease. At the same given flow rate on the main lane  $q_{\text{in}}$ , the lower the MB velocity  $v_{\text{MB}}$  is, the larger is on average the local speed decrease. For this reason, the on-ramp flow rate  $q_{\text{on}}$  is a characteristic of the on-ramp bottleneck that determines the so-called *strength* of the on-ramp bottleneck. Respectively, the MB velocity  $v_{\text{MB}}$  is a characteristic of the MB that determines the strength of the MB. In other words, for the same road infrastructure upstream of a bottleneck and the same flow rate  $q_{\text{in}}$ , the mean amplitude of the local speed decrease at a bottleneck is mostly determined by the bottleneck strength: The on-ramp flow rate  $q_{\text{on}}$  for the on-ramp bottleneck and the MB velocity  $v_{\text{MB}}$  for the MB.

This conclusion has been confirmed by many studies of vehicular traffic. In particular, from the diagrams of congested

TABLE I. Model parameters of vehicle motion in road lane often used in simulations.

|   |
|---|
| $\tau = 1 \text{ s}, d = 7.5 \text{ m}/\delta x,$   |
| $\delta x = 0.01 \text{ m}, \delta v = 0.01 \text{ m s}^{-1}, \delta a = 0.01 \text{ m s}^{-2},$                      |
| $v_{\text{free}} = 30 \text{ m s}^{-1}/\delta v, b = 1 \text{ m s}^{-2}/\delta a, a = 0.5 \text{ m s}^{-2}/\delta a,$ |
| $k = 3, p_1 = 0.3, p_b = 0.1, p_a = 0.17, p^{(0)} = 0.005,$   |
| $p_0(v_n) = 0.575 + 0.125 \min(1, v_n/v_{01}),$   |
| $p_2(v_n) = 0.48 + 0.32\Theta(v_n - v_{21}),$   |
| $v_{01} = 10 \text{ m s}^{-1}/\delta v, v_{21} = 15 \text{ m s}^{-1}/\delta v,$                                       |
| $a^{(0)} = 0.2a, a^{(a)} = a^{(b)} = a$   |

patterns at the on-ramp bottleneck and the MB [compare Fig. 11(c) of [39] for the pattern diagram at the on-ramp bottleneck with Fig. 8 of [39] for the pattern diagram at the MB] one can see the same sequence of physical effects, when at a given  $q_{\text{in}}$  the strength of the on-ramp bottleneck and the strength of the MB increases (respectively,  $q_{\text{on}}$  increases and  $v_{\text{MB}}$  decreases) beginning from lower bottleneck strengths at which free flow occurs to larger strengths at which traffic breakdown can occur with some probability  $P_{\text{FS}}^{(B)}$ .

This explains why in the methodology of this physical study of phase transitions at two different bottlenecks (the on-ramp bottleneck and the MB), as characteristics of the bottlenecks, the bottleneck strengths have been chosen and why a comparison of features of the phase transitions at the same flow rate  $q_{\text{in}}$  and the same probability of traffic breakdown  $P_{\text{FS}}^{(B)}$  has been made (Sec. II).

#### E. Role of model fluctuations in nucleation of phase transitions in vehicular traffic

The main objective of model fluctuations in the stochastic model (Secs. A 2 and A 3 of Appendix A) is the simulation of driver time delays. For example, the time delay in over-acceleration that explains the nucleation nature of the S  $\rightarrow$  J instability is simulated through the use of formula (A10), i.e., it is made through random fluctuations in vehicle acceleration (the physics of the simulation of the time delay in over-acceleration as well as of other driver time delays through the use of model fluctuations in the Kerner-Klenov model has been explained in the books [31,32]).

As can be seen from Secs. A 2 and A 3 of Appendix A, the maximal local speed decrease caused by model fluctuations is equal to  $a\tau = 0.5 \text{ m/s}$  (see Table I). This is considerably lower than amplitudes of the usual local speed decrease at bottlenecks measured in empirical traffic data that is on average within the range of 2 – 8 m/s.<sup>4</sup> For this reason, the nucleation of traffic breakdown (and other phase transitions) in empirical traffic data is observed due to the local speed decrease at bottlenecks (see Chap. 9 of [33]), rather than due to speed disturbance away from bottlenecks.

These empirical results of real traffic are incorporated in the Kerner-Klenov model: In the model, the nucleation of traf-

<sup>4</sup>Explanations of the occurrence of the local speed decrease at the bottlenecks have been given in Sec. VID. An empirical example of a large local speed decrease at a bottleneck can be seen in Fig. 4.3(c), (f) of [33].

fic breakdown (and other phase transitions) is realized through lane changing and vehicle merging at bottlenecks (see Secs. A 4<sup>5</sup> and A 5 of Appendix A), not through model fluctuations that are too small to be nuclei for the phase transitions. Indeed, the deterministic three-phase traffic model, in which no model fluctuations have been incorporated, show qualitatively the same diagram for traffic breakdown and congested patterns at the on-ramp bottleneck as those in the stochastic microscopic model used in the paper (compare Fig. 3(a) of [83] for the deterministic model with Fig. 5(a) of [39] for the stochastic model used in the paper). However, simulations with stochastic models are much quicker than with the deterministic one and, therefore, the stochastic model is more convenient for calculations of many vehicles moving on a long highway section during a long time interval.<sup>6</sup>

## F. Conclusion

By using the probability  $P_{FS}^{(B)}$  of traffic breakdown ( $F \rightarrow S$  transition) at the MB and on-ramp bottleneck as a baseline, we were able to compare the congested patterns formed at the two bottlenecks after traffic breakdown. Although the probability  $P_{FS}^{(B)}$  is identical at the MB and on-ramp bottleneck for a set of simulation parameters  $q_{in}$ ,  $v_{MB}$  and  $q_{on}$ , we observe a different behavior of the congested patterns at the two bottlenecks at a constant probability  $P_{FS}^{(B)}$  but for increasing velocity  $v_{MB}$  and decreasing traffic flow  $q_{on}$ , respectively (Figs. 6 and 7).

<sup>5</sup>To disclose the statistical physics of the development of Kerner's  $S \rightarrow F$  instability at the MB as well as to make the explanation of the physics as simple as possible, we have limited our paper by the consideration of a two-lane road. A generalization of paper results for a three-lane road system (and other multilane road systems) is out of the scope of this paper. This can be interesting task for further investigations of the  $S \rightarrow F$  instability.

<sup>6</sup>It would be interesting to derive a mesoscopic model that can capture the statistical features of traffic dynamics without a study of the dynamics behavior of vehicle trajectories made in the paper with the use of the analysis a relatively complex stochastic microscopic three-phase traffic model (Appendix A). The classical traffic flow instability that describes  $S \rightarrow J$  instability was introduced in the physics of traffic in the 1950s–1960s [1–7]. However, only about 35 years later first mesoscopic models for studies of the statistical features of traffic dynamics associated with the classical traffic flow instability have been developed. A well-known example is Bando *et al.* optimal velocity model [101,102] and studies of the statistical physics of moving jam emergence with this model (e.g., [12–14,16] and references therein). The first stochastic microscopic three-phase traffic model that can show the nucleation nature of traffic breakdown ( $F \rightarrow S$  transition at a bottleneck) was introduced in 2002 [37]. Unfortunately, in the world literature there are still no mesoscopic models that can capture the statistical features of traffic dynamics associated with the nucleation nature of the  $F \rightarrow S$  transition (traffic breakdown) at the bottleneck. In other words, there are no mesoscopic models for the  $S \rightarrow F$  instability whose competition with the speed adaptation governs the nucleation nature of traffic breakdown. The development of such a mesoscopic model legitimates a separate scientific study that is out of the scope of this paper. We believe that such a model development can be very interesting task for further investigations.

We revealed that this is linked to the movement of the MB. As is generally the case for synchronized flow, the downstream front is fixed at the bottleneck, which in case of the MB leads to a moving downstream front and to a dilution of synchronized flow. The mean space gap  $\bar{g}^{(S)}$  between the vehicles inside synchronized flow is linked to the velocity  $v_{MB}$  of the MB (Fig. 12). An increase in the velocity  $v_{MB}$  leads to a stronger dilution of synchronized flow, hence to an increase in the mean space gap  $\bar{g}^{(S)}$ . While we observe the dilution of synchronized flow at the MB, we do not observe the same effect at the on-ramp bottleneck. This is because, in contrast with the MB, at a given probability  $P_{FS}^{(B)}$  of traffic breakdown ( $F \rightarrow S$  transition) at the on-ramp bottleneck the flow rate  $q_{on}$  does not have a significant influence on the mean space gap  $\bar{g}^{(S)}$ .

The dilution of synchronized flow at the MB has a significant influence on the stochastic physical features of the  $S \rightarrow F$  instability (Fig. 15). With an increase in the mean space gap  $\bar{g}^{(S)}$ , a smaller amplitude of a speed peak (i.e., a local speed increase in synchronized flow) is necessary for it to become a nuclei for an  $S \rightarrow F$  instability and the probability for a speed peak to induce a growing speed wave increases. This leads to a dependence of the probability  $P_{SF}$  of an  $S \rightarrow F$  instability on the velocity  $v_{MB}$  of the MB: The probability  $P_{SF}$  increases with the velocity  $v_{MB}$  (Fig. 10). In turn, the probability  $P_{SJ}$  of an  $S \rightarrow J$  instability, which dominates the synchronized flow for low velocities  $v_{MB}$ , decreases with the velocity  $v_{MB}$  (Fig. 13). Furthermore, we identified an interval of the velocity  $v_{MB}$  or the mean space gap  $\bar{g}^{(S)}$ , respectively (Figs. 14 and 15), where there are three possible outcomes for the synchronized flow at the MB: interruption by an  $S \rightarrow F$  instability, interruption by an  $S \rightarrow J$  instability, or no interruption (Fig. 16).

In contrast, the  $S \rightarrow J$  instability at the on-ramp bottleneck dominates the synchronized flow for the observed parameter space as there is no dilution of synchronized flow. This explains the observed difference between the congested patterns at the MB and on-ramp bottleneck.

## ACKNOWLEDGMENTS

We thank our partners for their support in the project “LUKAS–Lokales Umfeldmodell für das Kooperative, Automatisierte Fahren in komplexen Verkehrssituationen” funded by the German Federal Ministry for Economic Affairs and Climate Action.

## APPENDIX A: KERNER-KLENOV STOCHASTIC MICROSCOPIC TRAFFIC FLOW MODEL USED FOR SIMULATIONS

### 1. Update rules of vehicle motion in road lane

For simulations made in this paper, we used the Kerner-Klenov stochastic microscopic model [37,39–41,88] in the framework of the three-phase traffic theory. The cause of the use of a microscopic model of human driving vehicles in the framework of the three-phase traffic theory has been explained

in [30–32]. Update rules of motion of human driving vehicles are<sup>7</sup>

$$v_{n+1} = \max(0, \min(v_{\text{free}}, \tilde{v}_{n+1} + \xi_n, v_n + a\tau, v_{s,n})), \quad (\text{A1})$$

$$x_{n+1} = x_n + v_{n+1}\tau, \quad (\text{A2})$$

where the index  $n$  corresponds to discrete time  $\tau n$ ,  $n = 0, 1, \dots, \tau = 1$  s,  $v_n$  is the vehicle speed at time step  $n$ ,  $a$  is the maximum acceleration and  $\tilde{v}_{n+1}$  is the vehicle speed without speed fluctuations  $\xi_n$ :

$$\tilde{v}_{n+1} = \min(v_{\text{free}}, v_{s,n}, v_{c,n}), \quad (\text{A3})$$

$$v_{c,n} = \begin{cases} v_n + \Delta_n & \text{at } g_n \leq G_n, \\ v_n + a_n\tau & \text{at } g_n > G_n, \end{cases} \quad (\text{A4})$$

$$\Delta_n = \max(-b_n\tau, \min(a_n\tau, v_{\ell,n} - v_n)), \quad (\text{A5})$$

where  $g_n = x_{\ell,n} - x_n - d$  is a space gap between two vehicles following each other, the subscript  $\ell$  marks variables related to the preceding vehicle,  $v_{s,n}$  is a safe speed at time step  $n$ ,  $v_{\text{free}}$  is the free flow speed in free flow,  $\xi_n$  describes the speed fluctuations,  $g_n$  is a space gap between two vehicles following each other, and  $G_n$  is the synchronization space gap; all vehicles have the same length  $d$ . While explanations of the physics of the safe speed  $v_{s,n}$  that can be found in Appendix A of [32] seems to be not important for the paper understanding, explanations of model fluctuations are important and, therefore, we discuss them below.

## 2. Model speed fluctuations

In the model [39,41], random vehicle deceleration and acceleration are applied depending on whether the vehicle decelerates or accelerates, or else maintains its speed:

$$\xi_n = \begin{cases} \xi_a & \text{if } S_{n+1} = 1 \\ -\xi_b & \text{if } S_{n+1} = -1 \\ \xi^{(0)} & \text{if } S_{n+1} = 0. \end{cases} \quad (\text{A6})$$

State-of-vehicle motion  $S_{n+1}$  in (A6) is determined by formula:

$$S_{n+1} = \begin{cases} -1 & \text{if } \tilde{v}_{n+1} < v_n \\ 1 & \text{if } \tilde{v}_{n+1} > v_n \\ 0 & \text{if } \tilde{v}_{n+1} = v_n. \end{cases} \quad (\text{A7})$$

<sup>7</sup>In a discrete model version of the Kerner-Klenov stochastic microscopic three-phase model used for all simulations, a discretized space coordinate with a small enough value of the discretization space interval  $\delta x$  is used [41]. Consequently, the vehicle speed and acceleration (deceleration) discretization intervals are  $\delta v = \delta x/\tau$  and  $\delta a = \delta v/\tau$ , respectively, where  $\tau$  is the time step. Because in the discrete model version discrete (and dimensionless) values of space coordinate, speed, and acceleration are used, which are measured respectively in values  $\delta x$ ,  $\delta v$ , and  $\delta a$ , and time is measured in values of  $\tau$ , value  $\tau$  in all formulas is assumed to be the dimensionless value  $\tau = 1$ .

In (A6),  $\xi_b$ ,  $\xi^{(0)}$ , and  $\xi_a$  are random sources for deceleration and acceleration that are as follows:

$$\xi_b = a^{(b)}\tau\Theta(p_b - r), \quad (\text{A8})$$

$$\xi^{(0)} = a^{(0)}\tau \begin{cases} -1 & \text{if } r < p^{(0)} \\ 1 & \text{if } p^{(0)} \leq r < 2p^{(0)} \wedge v_n > 0 \\ 0 & \text{otherwise,} \end{cases} \quad (\text{A9})$$

$$\xi_a = a^{(a)}\tau\Theta(p_a - r), \quad (\text{A10})$$

$p_b$  is probability of random vehicle deceleration,  $p_a$  is probability of random vehicle acceleration,  $p^{(0)}$  and  $a^{(0)} \leq a$  are constants,  $r = \text{rand}(0, 1)$ ,  $\Theta(z) = 0$  at  $z < 0$  and  $\Theta(z) = 1$  at  $z \geq 0$ , and  $a^{(a)}$  and  $a^{(b)}$  are model parameters (see Table I).

## 3. Stochastic time delays of acceleration and deceleration

To simulate time delays either in vehicle acceleration or in vehicle deceleration,  $a_n$  and  $b_n$  in (A4) and (A5) are taken as the following stochastic functions [39,41]:

$$a_n = a\Theta(P_0 - r_1), \quad (\text{A11})$$

$$b_n = a\Theta(P_1 - r_1), \quad (\text{A12})$$

$$P_0 = \begin{cases} p_0 & \text{if } S_n \neq 1 \\ 1 & \text{if } S_n = 1, \end{cases} \quad (\text{A13})$$

$$P_1 = \begin{cases} p_1 & \text{if } S_n \neq -1 \\ p_2 & \text{if } S_n = -1, \end{cases} \quad (\text{A14})$$

$r_1 = \text{rand}(0, 1)$ ,  $p_1$  is constant, and  $p_0 = p_0(v_n)$  and  $p_2 = p_2(v_n)$  are speed functions (see Table I).

## 4. Lane changing rules for two-lane road

As in other models of lane changing on a two-lane road (e.g., [103]), in the model a vehicle changes lane with probability  $p_c$  if some incentive lane changing rules together with some safety conditions for lane changing are satisfied.

Incentive lane changing rules from the right lane to the left lane ( $R \rightarrow L$ ) and from the left lane to the right lane ( $L \rightarrow R$ ) for lane changing are chosen similar to those of [103]:

$$R \rightarrow L: v_n^+ \geq v_{\ell,n} + \delta_1 \wedge v_n \geq v_{\ell,n}, \quad (\text{A15})$$

$$L \rightarrow R: v_n^+ > v_{\ell,n} + \delta_1 \vee v_n^+ > v_n + \delta_1, \quad (\text{A16})$$

where  $\delta_1$  is constant.

Under these conditions, a vehicle changes the lane when the following safety conditions for lane changing are satisfied [39]:

$$g_n^+ > \min(v_n\tau, G_n^+), \quad (\text{A17})$$

$$g_n^- > \min(v_n^-\tau, G_n^-), \quad (\text{A18})$$

where

$$g_n^+ = x_n^+ - x_n - d, \quad g_n^- = x_n - x_n^- - d, \quad (\text{A19})$$

$$G_n^+ = G(v_n, v_n^+), \quad G_n^- = G(v_n^-, v_n), \quad (\text{A20})$$

$G(u, w)$  is a synchronization space gap that is given by

$$G(u, w) = \max(0, [k\tau u + a^{-1}u(u - w)]), \quad (\text{A21})$$

TABLE II. Parameters of lane changing often used in simulations.

|  |
|--|
| $\delta_l = 1 \text{ m s}^{-1}/\delta v, L_a = 80 \text{ m}/\delta x, p_c = 0.2$ |
|--|

where  $k > 1$  is constant and  $\lfloor z \rfloor$  denotes the integer part of  $z$ .

In all formulas here and below, the superscripts  $+$  and  $-$  in variables, parameters, and functions denote the preceding vehicle and the trailing vehicle in the “target” (neighboring) lane, respectively (the target lane is the lane into which the vehicle wants to change). In conditions  $R \rightarrow L$  (A15) and  $L \rightarrow R$  (A16), the value  $v_n^+$  at  $g_n^+ > L_a$  and the value  $v_{\ell,n}$  at  $g_n > L_a$  are replaced by  $\infty$ , where  $L_a$  is a constant (see Table II).

### 5. Models of bottlenecks

Models of the on-ramp bottleneck [39] and the MB [88] are considered in Fig. 2. Within the merging region of the on-ramp bottleneck of length  $L_m$  [Fig. 2(b)] vehicles can merge onto the main lane from the on-ramp lane. Upstream of the merging region vehicles move in accordance with the model of Sec. A 1. The maximal speed of vehicles is  $v_{\text{free}} = v_{\text{free on}}$ .

A model of an MB is shown in Fig. 2(a). It is assumed [88] that there is a slow vehicle which maximum speed  $v_{\text{MB}}$  is smaller than the maximum speed of other vehicles:  $v_{\text{MB}} < v_{\text{free}}$ . The slow vehicle that moves in the right lane [Fig. 2(a)] causes an MB. If a vehicle moves at the speed  $v > v_{\text{MB}}$  in the right lane upstream of the slow vehicle, then the vehicle tries to changes from the right lane to the left lane within a merging region of the MB of length  $L_M$ . This merging region of the MB moves at the speed  $v_{\text{MB}}$  [Fig. 2(a)].

For all bottlenecks, when a vehicle is within the merging region of a bottleneck, the vehicle takes into account the space gaps to the preceding vehicles and their speeds in both the current and target lanes. Respectively, instead of formula (A4), in (A1) for the speed  $v_{c,n}$  the following formula is used [39,88]:

$$v_{c,n} = \begin{cases} v_n + \Delta_n^+ & \text{at } g_n^+ \leq G(v_n, \hat{v}_n^+) \\ v_n + a_n \tau & \text{at } g_n^+ > G(v_n, \hat{v}_n^+), \end{cases} \quad (\text{A22})$$

$$\Delta_n^+ = \max(-b_n \tau, \min(a_n \tau, \hat{v}_n^+ - v_n)), \quad (\text{A23})$$

$$\hat{v}_n^+ = \max(0, \min(v_{\text{free}}, v_n^+ + \Delta v_r^{(2)})), \quad (\text{A24})$$

$\Delta v_r^{(2)}$  is constant (see Table III).

As in lane changing rules (Sec. A 4), the superscripts  $+$  and  $-$  in variables, parameters and functions denote the preceding vehicle and the trailing vehicle in the target lane, respectively. The safe speed  $v_{s,n}$  in (A1), (A3) for the vehicle that is the

TABLE III. Parameters of models of bottlenecks used in simulations.

|  |
|--|
| $L_M = L_m = 0.3 \text{ km}/\delta x,$                 |
| $v_{\text{free on}} = 22.2 \text{ m s}^{-1}/\delta v,$ |
| $\Delta v_r^{(2)} = 5 \text{ m s}^{-1}/\delta v,$      |
| $\Delta v_r^{(1)} = 10 \text{ m s}^{-1}/\delta v$      |

TABLE IV. Conditions for the detection of phase transition points along a single-vehicle trajectory.

| Phase transition point | Condition for velocity | Condition for time interval |
|------------------------|------------------------|-----------------------------|
| F <sub>S</sub>         | $v < v_{\text{FS}}$    | $T > T_{\text{FS}}$         |
| S <sub>F</sub>         | $v > v_{\text{SF}}$    | $T > T_{\text{SF}}$         |
| S <sub>J</sub>         | $v < v_{\text{SJ}}$    | $T > T_{\text{SJ}}$         |
| J <sub>S</sub>         | $v > v_{\text{JS}}$    | $T > T_{\text{JS}}$         |

closest one to the end of on ramp is chosen in the form

$$v_{s,n} = \lfloor v^{(\text{safe})}(x_{\text{on}}^{(e)} - x_n, 0) \rfloor. \quad (\text{A25})$$

Vehicle merging at bottlenecks occurs, when safety conditions (\*) or safety conditions (\*\*) are satisfied [39,88]. Safety conditions (\*) are as follows:

$$g_n^+ > \min(\hat{v}_n \tau, G(\hat{v}_n, v_n^+)), \quad (\text{A26})$$

$$g_n^- > \min(v_n^- \tau, G(v_n^-, \hat{v}_n)),$$

$$\hat{v}_n = \min(v_n^+, v_n + \Delta v_r^{(1)}), \quad (\text{A27})$$

$\Delta v_r^{(1)} > 0$  is constant (see Table III). Safety conditions (\*\*) are as follows:

$$x_n^+ - x_n^- - d > g_{\text{target}}^{(\min)}, \quad (\text{A28})$$

where

$$g_{\text{target}}^{(\min)} = \lfloor \lambda_b v_n^+ + d \rfloor. \quad (\text{A29})$$

Contrary to [32], rather than a constant value  $\lambda_b$  in (A29), in this paper we have used

$$\lambda_b = \begin{cases} 0.75 & \text{at } v_n \geq v_{\text{pinch}}, \\ 0.4 & \text{at } v_n < v_{\text{pinch}}, \end{cases} \quad (\text{A30})$$

where  $v_{\text{pinch}}$  is a threshold velocity for the pinch region inside synchronized flow chosen as 10 m/s. This leads to more lane changes inside synchronized flow and a stronger synchronization of the velocities between the multiple lanes.

In addition to conditions (A28), the safety condition (\*\*) includes the condition that the vehicle should pass the midpoint:

$$x_n^{(m)} = \lfloor (x_n^+ + x_n^-)/2 \rfloor \quad (\text{A31})$$

TABLE V. Threshold parameters for the detection of the three traffic phases.

| Threshold       | Value   |
|-----------------|---------|
| $v_{\text{FS}}$ | 75 km/h |
| $T_{\text{FS}}$ | 5 s     |
| $v_{\text{SF}}$ | 75 km/h |
| $T_{\text{SF}}$ | 3 s     |
| $v_{\text{SJ}}$ | 10 km/h |
| $T_{\text{SJ}}$ | 5 s     |
| $v_{\text{JS}}$ | 10 km/h |
| $T_{\text{JS}}$ | 3 s     |

TABLE VI. Conditions for the detection of  $S \rightarrow F$  and  $S \rightarrow J$  instabilities.

| Instability       | Condition for velocity    | Condition for time interval |
|-------------------|---------------------------|-----------------------------|
| $S \rightarrow F$ | $v \geq v_{SF}^{(inst.)}$ | $T \geq T_{SF}^{(inst.)}$   |
| $S \rightarrow J$ | $v \leq v_{SJ}^{(inst.)}$ | $T \geq T_{SJ}^{(inst.)}$   |

between two neighboring vehicles in the target lane, i.e., conditions:

$$\begin{aligned}
 & x_{n-1} < x_{n-1}^{(m)} \quad \text{and} \quad x_n \geq x_n^{(m)} \\
 & \text{or} \\
 & x_{n-1} \geq x_{n-1}^{(m)} \quad \text{and} \quad x_n < x_n^{(m)}
 \end{aligned} \tag{A32}$$

should also be satisfied. The vehicle speed after vehicle merging is equal to

$$v_n = \hat{v}_n. \tag{A33}$$

Under conditions (\*), the vehicle coordinates  $x_n$  remains the same. Under conditions (\*\*), the vehicle coordinates  $x_n$  are equal to

$$x_n = x_n^{(m)}. \tag{A34}$$

#### APPENDIX B: METHOD FOR DETECTION OF TRAFFIC PHASES

For the detection of the traffic phases F, S, and J we used the method developed in [35] for real-life traffic data and adapted it to simulation data.

The method determines phase transition points along the trajectories of single vehicles, by examining the vehicle speed in dependence of time. Since there are no direct phases transitions between free flow and wide-moving jams, we have four possible phase transition points:  $F_S$  for an  $F \rightarrow S$  transition,  $S_F$  for an  $S \rightarrow F$  transition,  $S_J$  for an  $S \rightarrow J$  transition, and  $J_S$  for an  $J \rightarrow S$  transition. If the speed  $v$  along a single vehicle trajectory satisfies a certain condition for a consecutive time interval  $T$ , which has to be larger than a certain threshold, the corresponding phase transition point is detected (Table IV). For example, if the speed  $v$  of a vehicle starting in free flow is lower than the threshold  $v_{FS}$  for at least a consecutive time interval  $T$  longer than  $T_{FS}$ , a phase transition point  $F_S$  is detected at the beginning of the time interval  $T$  and at the corresponding position of the vehicle. This is done for all vehicles inside the simulation. The multitude of detected phase transition points allows the depiction of the traffic phases. Thresholds  $v_{FS}$ ,  $T_{FS}$ ,  $v_{SF}$ ,  $T_{SF}$ ,  $v_{SJ}$ ,  $T_{SJ}$ ,  $v_{JS}$ , and  $T_{JS}$ , are listed in Table V.

#### APPENDIX C: METHOD FOR DETECTION OF TRAFFIC BREAKDOWN ( $F \rightarrow S$ TRANSITION)

For the detection of traffic breakdown we used virtual detectors, placed along the left main lane, and measured the speeds of vehicles passing them. If the detected vehicle speeds are less than 75 km/h for a consecutive time interval  $T$ , which has to be larger than a certain threshold, a traffic breakdown is detected.

 TABLE VII. Threshold parameters for the detection of  $S \rightarrow F$  and  $S \rightarrow J$  instabilities.

| Threshold          | Value   |
|--------------------|---------|
| $v_{SF}^{(inst.)}$ | 78 km/h |
| $T_{SF}^{(inst.)}$ | 20 s    |
| $v_{SJ}^{(inst.)}$ | 10 km/h |
| $T_{SJ}^{(inst.)}$ | 20 s    |

For the on-ramp bottleneck, we used one stationary virtual detector placed 150 m upstream of the merging region  $L_m$  [Fig. 2(b)]. The threshold value for the time interval  $T$  is 300 s. For the MB, we used two types of virtual detectors: A moving one and multiple stationary ones. The moving one is placed at a constant distance of 150 m upstream of the MB and therefore moves with the MB at the same speed  $v_{MB}$  [Fig. 2(a)]. The threshold value for the time interval  $T$  is 300 s, the same as for the on-ramp bottleneck detector. The stationary detectors for the MB are placed equidistant (distance of 1 km) along the left main lane and start the measurement as soon as the MB has moved passed them and is 1 km downstream from the detectors. The threshold value for the time interval  $T$  is 90 s.

For the on-ramp bottleneck, where we only observed GPs for the used simulation parameters in this paper (Figs. 6 and 7), one stationary detector is sufficient to detect traffic breakdowns. As was shown in this paper, at the MB we have a diverse variety of congested traffic patterns (Figs. 5–7). Therefore it is necessary to use the two types of detectors, described above. The moving detector is able to detect WSPs and GPs forming at the MB, while the multiple stationary detectors are able to detect MSPs.

#### APPENDIX D: METHOD FOR DETECTION OF $S \rightarrow F$ AND $S \rightarrow J$ INSTABILITIES

The method for detecting  $S \rightarrow F$  and  $S \rightarrow J$  instabilities in this paper is similar to the method deployed in [36]. For each time step after traffic breakdown ( $F \rightarrow S$  transition) has occurred the speeds  $v$  of each vehicle inside the synchronized flow are checked for an  $S \rightarrow F$  or an  $S \rightarrow J$  instability. To mitigate the effect of the upstream front of synchronized flow and of the merging regions at the MB and on-ramp bottleneck, only the speeds  $v$  of vehicles are considered, which satisfy following conditions:

- (1) The vehicle is upstream of the merging region (Fig. 2).
- (2) The vehicle is 500 m downstream of the upstream front of synchronized flow.
- (3) The vehicle was at least for 30 s inside synchronized flow.

An  $S \rightarrow F$  instability is detected, when for a consecutive time interval  $T$  longer or equal than threshold  $T_{SF}^{(inst.)}$  the speed  $v$  of at least one vehicle is larger or equal than threshold  $v_{SF}^{(inst.)}$ . Similarly, an  $S \rightarrow J$  instability is detected, when for a consecutive time interval  $T$  longer or equal than threshold  $T_{SJ}^{(inst.)}$  the speed  $v$  of at least one vehicle is less or equal than threshold  $v_{SJ}^{(inst.)}$  (Table VI). Thresholds  $T_{SF}^{(inst.)}$ ,  $v_{SF}^{(inst.)}$ ,  $T_{SJ}^{(inst.)}$ , and  $v_{SJ}^{(inst.)}$  are listed in Table VII.

- [1] R. E. Chandler, R. Herman, and E. W. Montroll, *Oper. Res.* **6**, 165 (1958).
- [2] R. Herman, E. W. Montroll, R. B. Potts, and R. W. Rothery, *Oper. Res.* **7**, 86 (1959).
- [3] D. C. Gazis, R. Herman, and R. B. Potts, *Oper. Res.* **7**, 499 (1959).
- [4] D. C. Gazis, R. Herman, and R. W. Rothery, *Oper. Res.* **9**, 545 (1961).
- [5] E. Kometani and T. Sasaki, *J. Oper. Res. Soc. Jpn.* **2**, 11 (1958).
- [6] E. Kometani and T. Sasaki, *Oper. Res.* **7**, 704 (1959).
- [7] E. Kometani and T. Sasaki, *Oper. Res. Soc. Jpn.* **3**, 176 (1961).
- [8] E. Kometani and T. Sasaki, in *Theory of Traffic Flow*, edited by R. Herman (Elsevier, Amsterdam, 1961), pp. 105–119.
- [9] G. F. Newell, *Oper. Res.* **9**, 209 (1961).
- [10] G. F. Newell, in *Proc. Second Internat. Symp. on Traffic Road Traffic Flow* (OECD, London, 1963), pp. 73–83.
- [11] K. Nagel and M. Schreckenberg, *J. Phys. I France* **2**, 2221 (1992).
- [12] D. Chowdhury, L. Santen, and A. Schadschneider, *Phys. Rep.* **329**, 199 (2000).
- [13] D. Helbing, *Rev. Mod. Phys.* **73**, 1067 (2001).
- [14] T. Nagatani, *Rep. Prog. Phys.* **65**, 1331 (2002).
- [15] K. Nagel, P. Wagner, and R. Woessler, *Oper. Res.* **51**, 681 (2003).
- [16] A. Schadschneider, D. Chowdhury, and K. Nishinari, *Stochastic Transport in Complex Systems* (Elsevier Science, New York, 2011).
- [17] M. Treiber and A. Kesting, *Traffic Flow Dynamics*, (Springer, Berlin, 2013).
- [18] W. D. Ashton, *The Theory of Traffic Flow* (Methuen & Co., London and John Wiley & Sons, New York, 1966).
- [19] D. L. Gerlough and M. J. Huber, Traffic Flow Theory Special Report 165, Transportation Research Board, Washington, DC (1975).
- [20] D. C. Gazis, *Traffic Theory* (Springer, Berlin, 2002).
- [21] J. Barceló, editor, *Fundamentals of Traffic Simulation* (Springer, Berlin, 2010).
- [22] L. Elefteriadou, *An Introduction to Traffic Flow Theory* (Springer, Berlin, 2014).
- [23] D. Ni, *Traffic Flow Theory: Characteristics, Experimental Methods, and Numerical Techniques* (Elsevier, Amsterdam, 2015).
- [24] F. Kessels, *Traffic Flow Modelling* (Springer, Berlin, 2019).
- [25] B. S. Kerner and P. Konhäuser, *Phys. Rev. E* **48**, R2335 (1993).
- [26] B. S. Kerner and P. Konhäuser, *Phys. Rev. E* **50**, 54 (1994).
- [27] B. S. Kerner, *Trans. Res. Rec.* **1678**, 160 (1999); B. S. Kerner, in *Transportation and Traffic Theory*, edited by A. Ceder (Elsevier Science, Amsterdam, 1999), pp. 147–171; *Phys. World* **12**, 25 (1999); *Trans. Res. Rec.* **1710**, 136 (2000); *Netw. Spat. Econ.* **1**, 35 (2001); *Phys. Rev. E* **65**, 046138 (2002); *Trans. Res. Rec.* **1802**, 145 (2002); *Math. Comput. Model.* **35**, 481 (2002).
- [28] B. S. Kerner, *J. Phys. A: Math. Gen.* **33**, L221 (2000); in *Traffic and Granular Flow '99: Social, Traffic and Granular Dynamics*, edited by D. Helbing, H. J. Herrmann, M. Schreckenberg, and D. E. Wolf (Springer, Heidelberg, 2000), pp. 253–284.
- [29] B. S. Kerner, *Phys. Rev. Lett.* **81**, 3797 (1998); in *Proc. of Third Int. Symp. on Highway Capacity*, edited by R. Rysgaard (Road Directorate, Ministry of Transport, Copenhagen, 1998), pp. 621–641.
- [30] B. S. Kerner, *The Physics of Traffic* (Springer, Berlin, 2004).
- [31] B. S. Kerner, *Introduction to Modern Traffic Flow Theory and Control* (Springer, Berlin, 2009).
- [32] B. S. Kerner, *Breakdown in Traffic Networks* (Springer, Berlin, 2017).
- [33] B. S. Kerner, *Understanding Real Traffic* (Springer, Cham, 2021).
- [34] B. S. Kerner, *Phys. Rev. E* **92**, 062827 (2015).
- [35] B. S. Kerner, H. Rehborn, R.-P. Schäfer, S. L. Klenov, J. Palmer, S. Lorkowski, and N. Witte, *Physica A* **392**, 221 (2013).
- [36] B. S. Kerner, *Phys. Rev. E* **100**, 012303 (2019).
- [37] B. S. Kerner and S. L. Klenov, *J. Phys. A: Math. Gen.* **35**, L31 (2002).
- [38] B. S. Kerner, S. L. Klenov, and D. E. Wolf, *J. Phys. A: Math. Gen.* **35**, 9971 (2002).
- [39] B. S. Kerner and S. L. Klenov, *Phys. Rev. E* **68**, 036130 (2003).
- [40] B. S. Kerner and S. L. Klenov, *J. Phys. A: Math. Gen.* **37**, 8753 (2004).
- [41] B. S. Kerner and S. L. Klenov, *Phys. Rev. E* **80**, 056101 (2009).
- [42] B. S. Kerner, *J. Phys. A: Math. Theor.* **41**, 215101 (2008).
- [43] B. S. Kerner, *Phys. Rev. E* **85**, 036110 (2012).
- [44] B. S. Kerner, in *Complex Dynamics of Traffic Management*, edited by B. S. Kerner, Encyclopedia of Complexity and Systems Science Series (Springer, New York, 2019), pp. 389–500.
- [45] L. C. Davis, *Phys. Rev. E* **69**, 016108 (2004).
- [46] H. K. Lee, R. Barlović, M. Schreckenberg, and D. Kim, *Phys. Rev. Lett.* **92**, 238702 (2004).
- [47] R. Jiang and Q.-S. Wu, *J. Phys. A: Math. Gen.* **37**, 8197 (2004).
- [48] K. Gao, R. Jiang, S.-X. Hu, B.-H. Wang, and Q.-S. Wu, *Phys. Rev. E* **76**, 026105 (2007).
- [49] L. C. Davis, *Physica A* **368**, 541 (2006).
- [50] L. C. Davis, *Physica A* **361**, 606 (2006).
- [51] L. C. Davis, *Physica A* **387**, 6395 (2008).
- [52] L. C. Davis, *Physica A* **388**, 4459 (2009).
- [53] L. C. Davis, *Physica A* **389**, 3588 (2010).
- [54] L. C. Davis, *Physica A* **391**, 1679 (2012).
- [55] A. Pottmeier, C. Thiemann, A. Schadschneider, M. Schreckenberg, in A. Schadschneider, T. Pöschel, R. Kühne, M. Schreckenberg, and D. E. Wolf, editors, *Traffic and Granular Flow '05* (Springer, Berlin, 2007), pp. 503–508.
- [56] X. G. Li, Z. Y. Gao, K. P. Li, and X. M. Zhao, *Phys. Rev. E* **76**, 016110 (2007).
- [57] H.-K. Lee and B.-J. Kim, *Physica A* **390**, 4555 (2011).
- [58] K. Hausken and H. Rehborn, *Game Theoretic Analysis of Congestion, Safety and Security*, Springer Series in Reliability Engineering (Springer, Berlin, 2015), pp. 113–141.
- [59] J.-f. Tian, C. Zhu, and R. Jiang, in *Complex Dynamics of Traffic Management*, 2nd ed., edited by B. S. Kerner, Encyclopedia of Complexity and Systems Science (Springer, New York, 2019), pp. 313–342.
- [60] J.-W. Zeng, Y.-S. Qian, Z. Lv, F. Yin, L. Zhu, Y. Zhang, and D. Xu, *Physica A* **574**, 125918 (2021).
- [61] J.-W. Zeng, Y.-S. Qian, S.-B. Yu, and X.-T. Wei, *Physica A* **530**, 121567 (2019).

- [62] H.-T. Zhao, L. Lin, C.-P. Xu, Z.-X. Li, and X. Zhao, *Physica A* **553**, 124213 (2020).
- [63] J. J. Wu, H. J. Sun, and Z. Y. Gao, *Phys. Rev. E* **78**, 036103 (2008).
- [64] H. Yang, J. Lu, X.-J. Hu, and J. Jiang, *Physica A* **392**, 4009 (2013).
- [65] H. Yang, X. Zhai, and C. Zheng, *Physica A* **509**, 567 (2018).
- [66] F. Siebel and W. Mauser, *Phys. Rev. E* **73**, 066108 (2006).
- [67] F. Rempe and P. Franek, U. Fastenrath, and K. Bogenberger, *Transp. Res. C* **85**, 644 (2017).
- [68] H. Rehborn and S. L. Klenov, in *Encyclopedia of Complexity and System Science*, edited by R. A. Meyers (Springer, Berlin, 2009), pp. 9500–9536.
- [69] H. Rehborn, S. L. Klenov, and M. Koller, in *Complex Dynamics of Traffic Management*, edited by B. S. Kerner, Encyclopedia of Complexity and Systems Science Series (Springer, New York, 2019), pp. 501–557.
- [70] H. Rehborn, S. L. Klenov, and J. Palmer, *Physica A* **390**, 4466 (2011).
- [71] H. Rehborn, S. L. Klenov, and J. Palmer, in *IEEE Intell. Veh. Sym. (IV)* (IEEE, New York, 2011), pp. 19–24.
- [72] H. Rehborn and M. Koller, *J. Adv. Transp.* **48**, 1107 (2014).
- [73] H. Rehborn, M. Koller, and S. Kaufmann, *Data-Driven Traffic Engineering: Understanding of Traffic and Applications Based on Three-Phase Traffic Theory* (Elsevier, Amsterdam, 2021).
- [74] H. Rehborn and J. Palmer, in *2008 Intelligent Vehicles Symposium* (IEEE, New York, 2008), pp. 186–191.
- [75] Y.-S. Qian, X. Feng, and J.-W. Zeng, *Physica A* **479**, 509 (2017).
- [76] J. P. L. Neto, M. L. Lyra, and C. R. da Silva, *Physica A* **390**, 3558 (2011).
- [77] X.-j. Hu, H. Liu, X. Hao, Z. Su, and Z. Yang, *Physica A* **563**, 125495 (2021).
- [78] X.-j. Hu, F. Zhang, J. Lu, M.-y. Liu, Y.-f. Ma, and Q. Wan, *Physica A* **527**, 121176 (2019).
- [79] X.-j. Hu, X.-t. Hao, H. Wang, Z. Su, and F. Zhang, *Physica A* **545**, 123725 (2020).
- [80] X.-j. Hu, L.-q. Qiao, X.-t. Hao, C.-x. Lin, and T.-h. Liu, *Physica A* **605**, 127962 (2022).
- [81] D.-J. Fu, Q.-L. Li, R. Jiang, and B.-H. Wang, *Physica A* **559**, 125075 (2020).
- [82] R. Borsche, M. Kimathi, and A. Klar, *Comput. Math. Appl.* **64**, 2939 (2012).
- [83] B. S. Kerner and S. L. Klenov, *J. Phys. A: Math. Gen.* **39**, 1775 (2006).
- [84] D. C. Gazis and R. Herman, *The Moving and ‘Phantom’ Bottle-necks* (IBM Thomas J. Watson Research Division, Yorktown Heights, NY, 1990).
- [85] D. C. Gazis and R. Herman, *Transp. Sci.* **26**, 223 (1992).
- [86] G. F. Newell, A moving bottleneck, Technical Report UCB-ITS-RR-93-3, Institute of Transportation Studies, University of California, Berkeley (1993).
- [87] G. F. Newell, *Transp. Res. B* **32**, 531 (1998).
- [88] B. S. Kerner and S. L. Klenov, *J. Phys. A: Math. Theor.* **43**, 425101 (2010).
- [89] D. Wegerle, B. S. Kerner, M. Schreckenberg, and S. L. Klenov, *J. Int. Transp. Sys.* **24**, 598 (2020).
- [90] S. L. Klenov, D. Wegerle, B. S. Kerner, and M. Schreckenberg, *Comput. Res. Model.* **13**, 319 (2021).
- [91] W. Huang, Y. Dülger, H. Rehborn, B. A. Bernhardt, and J. Xu, in *Proc. TRB 100th Annual Meeting*, TRB Paper TRBAM-21-01-261 (Transportation Research Board, Washington, DC, 2021).
- [92] B. S. Kerner, S. L. Klenov, and A. Hiller, *J. Phys. A: Math. Gen.* **39**, 2001 (2006).
- [93] B. S. Kerner, S. L. Klenov, and A. Hiller, *Nonlinear Dyn.* **49**, 525 (2007).
- [94] B. S. Kerner, S. L. Klenov, G. Hermanns, P. Hemmerle, H. Rehborn, and M. Schreckenberg, *Phys. Rev. E* **88**, 054801 (2013).
- [95] B. S. Kerner, P. Hemmerle, M. Koller, G. Hermanns, S. L. Klenov, H. Rehborn, and M. Schreckenberg, *Phys. Rev. E* **90**, 032810 (2014); P. Hemmerle, M. Koller, H. Rehborn, B. S. Kerner, and M. Schreckenberg, *IET Intell. Transp. Syst.* **10**, 122 (2016); G. Hermanns, P. Hemmerle, H. Rehborn, M. Koller, B. S. Kerner, and M. Schreckenberg, *Transp. Res. Record* **2490**, 47 (2015); P. Hemmerle, M. Koller, G. Hermanns, H. Rehborn, B. S. Kerner, and M. Schreckenberg, *Coll. Dyn.* **1**, A7 (2016).
- [96] B. S. Kerner, *Europhys. Lett.* **102**, 28010 (2013); *Physica A* **397**, 76 (2014); B. S. Kerner, S. L. Klenov, and M. Schreckenberg, *J. Stat. Mech.* (2014) P03001.
- [97] S. Kaufmann, B. S. Kerner, H. Rehborn, M. Koller, and S. L. Klenov, *Transp. Res. C* **86**, 393 (2018).
- [98] S.-E. Molzahn, B. S. Kerner, H. Rehborn, S. L. Klenov, and M. Koller, *IET Intel. Transp. Sys.* **11**, 604 (2017); Y. Dülger, S.-E. Molzahn, H. Rehborn, M. Koller, B. S. Kerner, D. Wegerle, M. Schreckenberg, M. Menth, and S. L. Klenov, *J. Intel. Transp. Sys.* **24**, 539 (2020).
- [99] R. Jiang, M. B. Hu, H. M. Zhang, Z. Y. Gao, B. Jia, Q. S. Wu, B. Wang, and M. Yang, *Plos ONE* **9**, e94351 (2014); R. Jiang, M. B. Hu, H. M. Zhang, Z. Y. Gao, B. Jia, and Q. S. Wu, *Transp. Res. B* **80**, 338 (2015); R. Jiang, C. J. Jin, H. M. Zhang, Y. X. Huang, J. F. Tian, W. Wang, M. B. Hu, H. Wang, and B. Jia, *Transp. Res. C* **94**, 83 (2018); Y. X. Huang, R. Jiang, H. M. Zhang, M. B. Hu, J. F. Tian, B. Jia, and Z. Y. Gao, *ibid.* **97**, 194 (2018).
- [100] S.-T. Zheng, R. Jiang, J.-f. Tian, X.-p. Li, M. Treiber, Z.-H. Li, L.-D. Gao, and B. Jia, *Transp. Res. C* **140**, 103729 (2022).
- [101] M. Bando, K. Hasebe, A. Nakayama, A. Shibata, and Y. Sugiyama, *Jpn. J. Appl. Math.* **11**, 203 (1994); *Phys. Rev. E* **51**, 1035 (1995).
- [102] M. Bando, K. Hasebe, A. Nakayama, A. Shibata, and Y. Sugiyama, *J. Phys. I France* **5**, 1389 (1995).
- [103] K. Nagel, D. E. Wolf, P. Wagner, and P. Simon, *Phys. Rev. E* **58**, 1425 (1998).